A VERSATILE TUNEABLE CURVELET-LIKE DIRECTIONAL FILTER WITH APPLICATION TO FRACTURE DETECTION IN TWO-DIMENSIONAL GPR DATA

Andreas Tzanis

Department of Geophysics and Geothermy,
National and Kapodistrian University of Athens,
Panepistimiopoli,
Zografou 15784,Greece.
E-mail: atzanis@geol.uoa.gr

Reference: Tzanis, A., 2017. A versatile tuneable curvelet-like directional filter with application to fracture detection in two-dimensional GPR data, *Signal Processing*, 132, 243-260; DOI: 10.1016/j.sigpro.2016.07.009.

Athens, May 2017

Abstract

The present work introduces a curvelet-like directional filter and discusses its application to edge detection in general images and fracture detection in GPR data. The filter is essentially a curvelet of adjustable anisotropy and orientation that can be tuned on any given (target) wavenumber; while retaining the properties of curvelets, it is not bound to the scaling rules of the Curvelet Frame but is individually steerable to any local trait of the data, hence it is dubbed "Curveletiform". Curveletiforms can be used in single- or multi-directional modes in a manner simple, computationally inexpensive and demonstrably efficient. GPR data generally contains straight or curved edge-like objects comprising reflections from planar interfaces and is notoriously susceptible to broadband noise. Fractures are an important class of interfaces as they determine the health state of rocks or man-made structures and are primary targets of GPR surveys in geotechnical, engineering and environmental applications. As demonstrated with examples, Curveletiforms can efficiently recover information of specific scale and geometry from straight or curved edges in general images. In GPR data they may distinguish reflections from small and large fractures, discriminate between groups of fractures, resolve fracture density and aid the assessment of damage in rocks and structures.

Keywords: Ground Probing Radar; Image Processing; Curvelet; Directional Filter; Edge Detection; Fracture Detection.

1. INTRODUCTION

The purpose of this presentation is to introduce an effective and efficient method of geometrical information retrieval from noisy images containing straight or curved objects (edges), with particular emphasis placed on the problem of recovering features associated with specific scales and geometry orientation. The technique will be mainly demonstrated with an application to fracture detection and rock health assessment in noisy Ground Probing RADAR (GPR) data, a problem that to all intents and purposes is equivalent to the problem of edge detection. The next paragraph of this introduction comprises a short exposition of the constitution of GPR data, so as to justify why advanced edge detection methods are suitable for GPR data analysis (conversely, why GPR data is suitable for testing such methods). The remaining main part will review methods developed for the retrieval/manipulation of geometrical information from digital images and how they have inspired the formulation of the proposed technique.

The GPR is an almost indispensable means of imaging near surface structures and enjoys a very diverse and broad range of applications. GPR data essentially comprise recordings of the amplitudes of transient waves propagating in the Earth (*wavefield*). A GPR section (or B-scan), provides a two-dimensional spatio-temporal image of the transient wavefield which contains different arrivals corresponding to different interactions with wave scatterers (inhomogeneities) in the subsurface. Accordingly, two-dimensional GPR images comprise wavefronts scattered or reflected from small targets and planar or bending interfaces such as geological bedding, miscellaneous structural boundaries, cracks, fractures and joints, empty or filled cavities associated with jointing or faulting and other conceivable structural configurations. The second group of targets, especially fractures, are usually not good reflectors and are spatially localized; in geological, geotechnical, civil engineering, mining and environmental protection applications their detection is frequently a primary objective as their presence and density is always associated with the level of damage sustained by native rocks or construction materials. Wavefronts from fractures are longitudinally smooth, transversely oscillatory and generally associated with the geometry of their originating reflectors: in short, they are genuine (curved) edges. At the same time, GPR data is notoriously susceptible to noise. A variety of natural and artificial objects can cause unwanted reflections and scattering, including extraneous or reflected airwaves, critically refracted airwaves and groundwaves. Anthropogenic noise is worse and includes interference from power lines and telecommunication devices. Finally, there's systemic noise, frequently manifested as ringing (antenna self-clutter). In many cases, the noise has definite geometrical characteristics which should be factored into any noise excision procedure. Raw GPR data usually require post-acquisition processing, as in their original form they provide only approximate target shapes and depths.

There are several methods to de-noise two dimensional data, focus on single or multiple scales and extract geometrical information. Almost all of them have been described in the excellent and comprehensive review of Jacques et al. [1]. The requirement to manipulate geometrical (orientation-dependent) information classifies suitable methods in two general categories: Directional Filters (or Directional Wavelets) and multi-directional Multi-Resolution Analysis (MRA).

Directional Filters (Directional Wavelets) are used in texture analysis, edge detection, image data compression, motion analysis, and image (signal) enhancement. They generally comprise anisotropic 2-D waveforms based on steerable semi-orthogonal or orthogonal wavelet arrays, whose frequency and/or wavenumber localization can be manipulated by changing their scale and orientation. These include Steerable Wavelets [2, 3], Gabor wavelets [4 – 6] and B-Spline Wavelet Filters [7, 8]. These methods may successfully process information at arbitrarily fine scales and single orientations but do not allow for a different number of directions at each scale. In order to obtain multidirectional representation of the data at each scale, it is necessary to apply the same filter rotated to different angles (under adaptive control if necessary) and combine the outputs, as in [2] for Steerable Wavelets

and in [9] for Gabor Filters. Multidirectional applications of B-Spline Wavelet and Gabor Filters to the analysis of contaminated GPR data are given in [8, 10] and have met with remarkable success. In any case, the angular selectivity of the most advanced directional filter designs depends on a number of shaping parameters, the coordination of which is generally application-specific and requires experience.

Multi-Resolution Analysis, e.g. [11 – 12], is the design method of most of the practically relevant discrete wavelet transforms and the justification of the fast wavelet transform. MRA allows an image – formally a space $L^2(\mathbb{R}^2)$ – to be decomposed into a sequence of nested sub-images (subspaces) arranged in order of increasing detail (decreasing scale), so as to satisfy certain self-similarity conditions in space, as well as completeness and regularity relations. This provides a means to manipulate localized (specific scale) events but leave the rest of the data generally unscathed. MRA has been applied to reflection seismic and GPR data, with most of the relevant studies focusing on noise suppression in a time-frequency sense. The pertinent literature is not abundant, but is progressively expanding, e.g. [13 – 18].

Wavelet-based MRA methods are not efficient in processing geometrical information. Just as Fourier methods are unsuitable for (or inadaptable to) problems involving aperiodic phenomena, which has led to the advent of the wavelet transform, wavelets are isotropic and may successfully operate only on phenomena that are generally isotropic, except for local irregularities (isolated singularities at exceptional points). Wavelets are less than ideal for phenomena occurring on curves or sheets (i.e. with singularities on curves), as for instance, edges in two-dimensional images or wavefronts in a seismic or GPR record. This problem has been addressed by advanced MRA-like algorithms collectively referred to as the "*X-let Transform*". These include *ridgelets* [19, 20], *wedgelets* [21], *beamlets* [22], *bandlets* [23], *contourlets* [24], *wave atoms* [25], *surfacelets* [26] and others. It is also possible to combine *X*-lets with machine learning procedures for increased efficiency [e.g. 44, 45]. At any rate, the *X*-lets vary substantially in scope, properties and efficiency so that even their general characteristics are beyond summarizing herein: a comprehensive review can be found in [1]. Additional effective and versatile methods are the second generation *Curvelet Transform* [27 – 31] and its spin-offs, the *Shearlet Transform* [32] and the *Riplet Transform* [33]. These are designed to associate scale with orientation, yield optimally sparse representations of the data and have optimal reconstruction properties (see below). These very desirable characteristics of the Curvelet Transform lineage have motivated research into its suitability for GPR data processing [34] and have partially inspired the present investigation which will concentrate on the most fundamental design: the Curvelet.

Curvelets trace their origin in Harmonic Analysis, where they were introduced as expansions for asymptotic solutions of wave equations [19, 35]. In consequence, curvelets can be viewed as primitive and prototype waveforms – they are local in space or wavenumber and highly anisotropic as they obey

the parabolic scaling principle, according to which their width is proportional to the square of their length. Their anisotropic shape endows them with the capacity to detect curved objects at different angles and scales because curvelets at a given scale and orientation can only locally match with curves (edges, wavefronts etc.) of the same scale and orientation. The 2nd generation Curvelet Transform [27 – 31], comprises a multiscale and multidirectional expansion that formulates an *optimally sparse* representation of objects with edges, in the sense that there is no other representation of the same order *m* that can yield a better approximation [30]. Optimal sparsity also leads to optimal image reconstruction in severely ill-posed problems [36] and renders Curvelets particularly suitable for reconstruction problems with corrupted and/or missing data [31, 36].

The (Fast Discrete) Curvelet Transform was applied to the analysis of GPR data with notable success [34]. However, there is a small disadvantage in that the CT cannot be readily customized for specific high-precision applications because it is a *pyramidal decomposition* that partitions the Fourier plane into highly anisotropic and localized elements (curvelets), albeit in a rather inflexible manner, as detailed in the beginning of Section 2.1. At this point it suffices to state that in the CT formalism, if ρ and θ are the radial and azimuthal coordinates respectively, the Fourier plane is partitioned in concentric annuli (*coronae*) according to the rule $2^{j-1} \le \rho \le 2^{j+1}$, with each corona further partitioned into angular sectors according to the rule $\angle\theta \le 2^{-j/2}$ (*second dyadic decomposition*). This may affect operations in which "surgical" precision is desired. For example, objects whose Fourier-plane components straddle the boundaries of coronae and/or angular sectors may not be very effectively isolated because the predefined partitioning scheme will integrate information from a broader than necessary range of scales and angular spans. In addition, when the aspect ratio of the data matrix is high or low – e.g. too many columns with respect to rows as is often the case with GPR data – the angular partitioning becomes awkward and cumbersome, sometimes making impossible to analyse the data as a single matrix (image).

The above discussion indicates that a tuneable directional filter with all the nice and desirable properties of curvelets could be a useful addition to the arsenal of image processing, and GPR data processing in particular. The present work describes and applies a hybrid scheme in which the filter:

1. Retains the design characteristics and desirable microlocal properties of curvelets.
2. Is not bound to the scaling rules of the second dyadic decomposition but is automatically localizable and scalable (tuneable) around any pair of coordinates in the Fourier plane, hence any particular trait in the data.
3. Its design and construction is (almost) independent of shaping parameters so that it can be applied by users inexperienced in advanced filters and image processing schemes.
4. Can be applied in single- or multi-directional sense and in computationally inexpensive fashion.

The construction and basic properties of this filter, which is dubbed "*curveletiform*" for reasons soon to be clear, will be presented in Section 2 albeit in a succinct and practical manner. As will be

demonstrated with examples in Sections 3 and 4, the filter is particularly suitable for use in the detection of linear and curved objects such as edges and, in the case of GPR data, reflections from fractures. A brief recapitulation and discussion in Section 5 will conclude the presentation.

2. THE "CURVELETIFORM" FILTER

2.1 The Curvelet Frame and Transform

A Curvelet Frame is a wave packet frame on $L^2(\mathbb{R}^2)$ based on a second dyadic decomposition. It comprises an extension of the isotropic MRA concept to include anisotropic scaling and directionality (angular dependence) while maintaining rotational invariance. The curvelet frame is based on a template (basic) curvelet from which it can be generated by translation, dilation and rotation. The elements of the curvelet family provide a partition (tiling) of the two-dimensional Fourier plane.

Consider a function $f(\mathbf{x}) \in L^2(\mathbb{R}^2)$ with $\mathbf{x} = [x_1 \; x_2]^T$. Next, consider the Fourier transform pair $f(\mathbf{x}) \leftrightarrow F(\boldsymbol{\xi})$ where $\boldsymbol{\xi} = [\xi_1 \; \xi_2]^T$ and ξ_j represent Fourier domain coordinates (e.g. wavenumber or/and frequency). Let $\rho = |\boldsymbol{\xi}|$ be the radial coordinate and $\Theta = \arctan(\xi_1, \; \xi_2)$ be the azimuthal coordinate in the ξ-plane. Finally, consider a partition of the polar coordinate plane in concentric annuli (*coronae*) according to $2^{j-1} \le \rho \le 2^{j+1}$, with each corona further partitioned into angular sectors according to $\angle\Theta \le 2^{-j/2}$, so as to generate a set of *polar wedges* (Fig. 1a). The number of the wedges N_j increases like $2^{\lfloor j/2 \rfloor}$, where $\lfloor . \rfloor$ denotes the floor operator (integer part), and doubles in every second corona so that the width of the wedges is proportional to the square of their length: this is the so called *parabolic scaling* (Fig. 1b). Each of these wedges supports a curvelet as will be shown below.

Now, consider a *radial* window $W(\rho)$ and an *angular* window $V(t)$, which must be smooth, nonnegative and real-valued. W is supported in (1/2, 2) and obeys the *admissibility condition* $\sum_{j=-\infty}^{\infty} \left|W(2^{-j}\rho)\right|^2 = 1$ for $\rho > 0$. V is supported in $(-2\pi, \; 2\pi]$ and the corresponding admissibility condition is $\sum_{l=-\infty}^{\infty} V^2(t - 2\pi l) = 1$ for $t \in \mathbb{R}$.

The dilated basic curvelet in polar coordinates is given by

$$\Psi_{j,l=0,k=0}(\boldsymbol{\xi}) = 2^{-3j/4} W(2^{-j}\rho) \cdot V\left(\frac{2^{\lfloor j/2 \rfloor}\Theta}{2\pi}\right), \qquad \rho \ge 0, \quad \Theta \in [0, 2\pi), \quad j \in \mathbb{N}_0 . \tag{1}$$

Evidently, $W(2^{-j}\rho)$ admits ξ-values located in the corona $(2^{j-1}, 2^{j+1})$. Similarly, $V(2^{\lfloor j/2 \rfloor}\Theta)$ admits ξ-values located in the angular sector $(-\pi 2^{-\lfloor j/2 \rfloor}, \; \pi 2^{-\lfloor j/2 \rfloor})$ so that $\Psi_{j,0,0}(\boldsymbol{\xi})$ is bounded by a polar wedge as in Fig. 1. For increasing j and decreasing scale $2^{-j} \in (0, 1]$, the breadth of W is growing and the width of V is shrinking, so that the polar wedges $\Psi_{j,0,0}(\boldsymbol{\xi})$ become longer (see Fig. 1a and 1c): this is the effect of parabolic scaling. The complete ξ-domain curvelet family is generated from $\Psi_{j,0,0}$ by

dilation, rotation and translation according to $\Psi_{j,l,k}(\boldsymbol{\xi}) = \Psi_{j,0,0}\left(\mathbf{R}_{\theta_{j,l}}\boldsymbol{\xi}\right)\cdot\exp\left(-i\langle\mathbf{x}_{\mathbf{k}}^{j,l},\boldsymbol{\xi}\rangle\right)$, which in terms of the radial and angular windows assumes the form

$$\Psi_{j,l,k}(\boldsymbol{\xi}) = 2^{-3j/4}W(2^{-j}\rho)\cdot V\left(\frac{2^{\lfloor j/2\rfloor}}{2\pi}(\Theta-\theta_l)\right)\cdot\exp\left(-i\langle\mathbf{x}_{\mathbf{k}}^{j,l},\boldsymbol{\xi}\rangle\right). \qquad (2)$$

In Eq. (2), $\theta_{j,l} = 2\pi l\cdot 2^{-\lfloor j/2\rfloor}$, $l = 0,1,2,\ldots$, $0\le\theta_{j,l}<2\pi$, is a sequence of equi-spaced rotation angles whose number varies proportionally to $2^{\lfloor j/2\rfloor}$,

$$\mathbf{x}_{\mathbf{k}}^{j,l} = \mathbf{R}_{\theta_l}^{-1}\begin{bmatrix}2^{-j} & 0\\ 0 & 2^{-j/2}\end{bmatrix}\begin{bmatrix}k_1\\ k_2\end{bmatrix}$$

are scaled positions with $k_1,k_2\in\mathbb{Z}^2$ representing the translation parameters and

$$\mathbf{R}_{\theta_{j,l}} = \begin{bmatrix}\cos\theta_{j,l} & \sin\theta_{j,l}\\ -\sin\theta_{j,l} & \cos\theta_{j,l}\end{bmatrix},\qquad \mathbf{R}_{\vartheta}^{-1} = \mathbf{R}_{\vartheta}^{T} = \mathbf{R}_{-\theta},$$

is the rotation by $\theta_{j,l}$ radians. As evident, the support of $\Psi_{j,l,k}$ does not depend on the translation

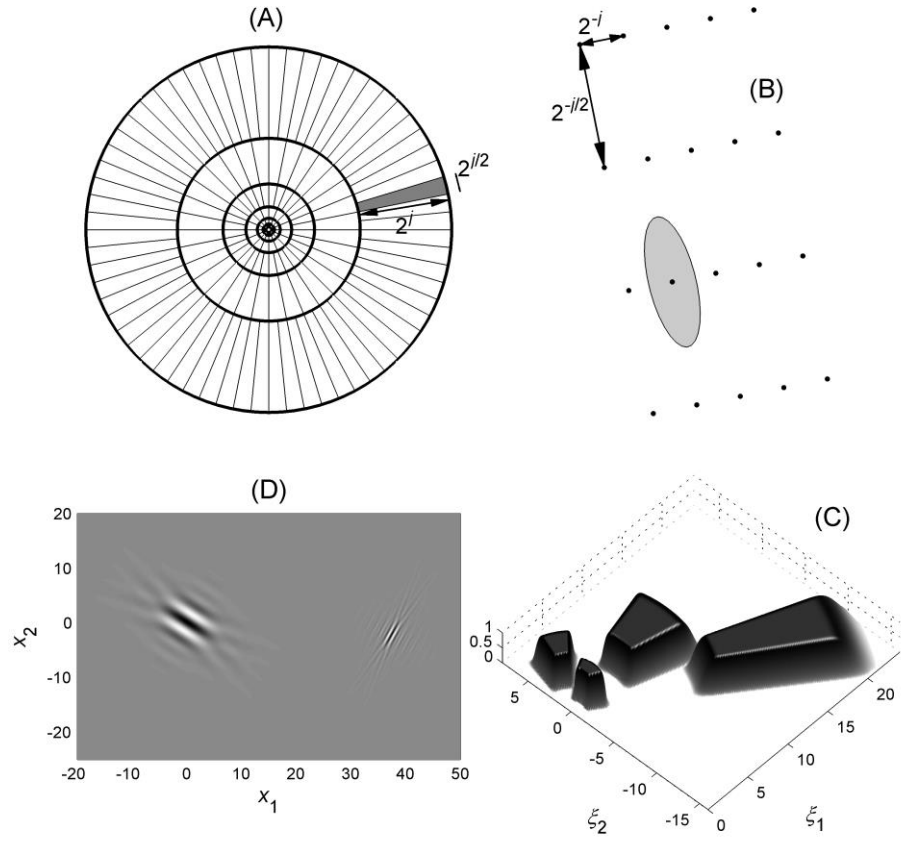

Figure 1. (a) Exemplary tiling of the ξ-plane in polar coordinates with parabolic scaling. The shaded area highlights a wedge supporting a curvelet. **(b)** Schematic representation of a Cartesian grid in the *x*-domain, associated with a ξ-domain wedge like the one highlighted in Fig. 1a; the scaling of the *x*-domain curvelets (schematically represented by the ellipse) is also parabolic. **(c)** Some ξ-domain curvelets in perspective view: from left to right they are {*j*=1, *l*=0}, {*j*=2, *l*=2}, {*j*=3, *l*=0} and {*j*=4, *l*=22}. **(d)** The *x*-domain curvelets {*j*=2, *l*=2} (left) and an arbitrarily translated version of {*j*=4, *l*=22} (right).

parameters. The angular window V isolates ξ-values in the sector $-\pi 2^{-\lfloor j/2 \rfloor} \le \Theta - \theta_{j,l} \le \pi 2^{-\lfloor j/2 \rfloor}$.

In the x-domain, the curvelet is a waveform defined by the Fourier Transform of Ψ:

$$\psi_{j,l,k}(\mathbf{x}) = \psi_{j,0,0}\left(\mathbf{R}_{\theta_l}(\mathbf{x} - \mathbf{x}_{\mathbf{k}}^{j,l})\right). \quad (3)$$

Because the support of $\Psi_{j,l,k}$ is independent of $\mathbf{k}$, the frequency localization of $\Psi_{j,l,0}$ is such that $\psi_{j,l,0}(\mathbf{x})$ decays rapidly outside a rectangle of size $2^{-j} \times 2^{-j/2}$ (major axis perpendicular to the polar angle $\theta_{j,l}$ as in Fig. 1b and 1d). Accordingly, the effective size of $\psi_{j,l,k}(\mathbf{x})$ will also obey parabolic scaling rules whereby *length* $\approx 2^{-j/2}$, *width* $\approx 2^{-j}$ so that *width* $\approx$ *length*^{2}. In addition, $\Psi_{j,0,0}$ is by construction supported away from the ξ_2 axis (where $\xi_1 = 0$) but near the ξ_1 axis (where $\xi_2 = 0$). Therefore, $\psi_{j,0,0}(\mathbf{x})$ oscillates in the x_2-direction and is low-pass in the x_1-direction, properties which are preserved during rotation and translation (e.g. Fig. 1d). Thus, at any scale 2^{-j} a curvelet is enveloped by a ridge with effective length $2^{-j/2}$ and width 2^{-j} and oscillates in a direction perpendicular to that ridge (Fig. 1d).

A last matter to be considered is the "hole" arising in the ξ-plane around zero, since the rotation of the basic curvelet is defined only for scales 2^{-j}. For a complete covering of the ξ-plane a non-directional (isotropic) low-pass element W_{j0} is required, which obeys $\left|W_{j_0}(\rho)\right|^2 + \sum_{j>j_0}\left|W(2^{-j}\rho)\right|^2 = 1$, so that *coarsest scale* curvelet will be $\Psi_{j_0}(\boldsymbol{\xi}) = 2^{-j_0} W_{j_0}\left(2^{-j_0}|\boldsymbol{\xi}|\right)$, and will admit a x-domain representation of the form $\psi_{j_0,k}(\mathbf{x}) = \psi_{j_0}(\mathbf{x} - 2^{-j_0}\mathbf{k})$.

Based on the above construction principles, a *curvelet coefficient* comprises the inner product between $f(x_1, x_2)$ and a curvelet $\psi_{j,l,k}$, $j > j_0$:

$$c(j,l,k) = \left\langle f, \psi_{j,l,k} \right\rangle = \int_{\mathbb{R}^2} f(\mathbf{x})\,\overline{\psi_{j,l,k}(\mathbf{x})}\,d\mathbf{x}. \quad (4)$$

The inverse continuous curvelet transform will then be defined by the reconstruction rule

$$f(\mathbf{x}) = \sum_{j \ge j_0, l, k} c(j,l,k)\,\psi_{j,l,k}(\mathbf{x}), \quad (5)$$

with the Parseval condition $\sum_{j,l,k}|c(j,l,k)|^2 = \|f\|^2_{L^2(\mathbb{R}^2)}$ holding for all $f \in L^2(\mathbb{R}^2)$ and guaranteeing a *tight frame* property. As a result of the parabolic scaling, the curvelet frame is an optimally sparse representation of functions that are smooth except for singularities along curves [37].

For objects with edges, specifically objects that are smooth except for discontinuities along general curves with bounded curvature (twice differentiable or C^2-continuous), the representation formulated by Eq. (4) and (5) is *optimally sparse* : it has been shown that if f_m is the m-order curvelet approximation to $f(\mathbf{x})$, the approximation error is $\|f - f_m\|_2^2 = O\left(m^{-2}[\log m]^3\right)$ and is optimal in the sense that there is no other representation of the same order that can yield a smaller asymptotic error [30]. This is far better than the $O(m^{-1})$ error afforded by the wavelet approximation. It also means that one may recover curved objects from noisy data by curvelet shrinkage (analogous to wavelet

shrinkage) and obtain a mean squared error far better than what is affordable with more traditional methods [36].

Optimal sparsity also leads to optimal image reconstruction in severely ill-posed problems. Curvelets possess *microlocal* properties, (i.e. localization properties dependent on both position and orientation), which render them particularly suitable for reconstruction problems with corrupted or missing data. Depending on the characteristics of noise, the curvelet expansion can be separated into a subset that can be recovered accurately, and one that cannot. The microlocal properties of the curvelets allow the recoverable part to be reconstructed with accuracy similar to the accuracy that would be feasible if the data was complete and noise-free. It has been shown in [31] that for statistical models which allow for C^2 objects to be recovered, there are simple algorithms based on shrinkage of curvelet biorthogonal decompositions that achieve optimal statistical rates of convergence, i.e. there is no other estimating procedure which can return a fundamentally better mean square error (approximation).

2.2 From Curvelet to Curveletiform

In order to mutate Curvelets into "Curveletiforms", it is first necessary to introduce explicit forms for the radial (W) and azimuthal (V) widows discussed in Section 2.1. Accordingly, consider the scaled *Meyer* windows, e.g. [38], pp. 126-128.

$$W(r) = \begin{cases} \cos\left[\frac{\pi}{2} w(5-6u)\right] & 2/3 \le r \le 5/6 \\ 1 & 5/6 \le r \le 4/3 \\ \cos\left[\frac{\pi}{2} w(3u-4)\right] & 4/3 \le r \le 5/3 \\ 0 & otherwise \end{cases}, \qquad r \in (1/2,\, 2)$$

and

$$V(u) = \begin{cases} 1, & |u| \le \frac{1}{3} \\ \cos\left[\frac{\pi}{2} w(3|u|-1)\right], & \frac{1}{3} \le |u| \le \frac{2}{3}, \\ 0, & othewise \end{cases} \qquad u \in (-2\pi,\, 2\pi]$$

with w satisfying

$$w(x) = \begin{cases} 0 & x \le 0 \\ 1 & x \ge 1 \end{cases}, \qquad w(x) + w(1-x) = 1, \qquad x \in \mathbb{R}.$$

In order to obtain smooth W and V, it is necessary to use smooth $w(x)$. Common forms of w are the polynomials $w(x) = 3x^2 - 2x^3$ or $w(x) = 5x^3 - 5x^4 + x^5$ in [0, 1], such that $w \in C^1(\mathbb{R})$ and $w \in C^2(\mathbb{R})$ respectively. It is also possible to obtain arbitrarily smooth W and V when

$$w(x) \begin{cases} 0 & x \le 0 \\ \dfrac{s(x-1)}{s(x-1) + s(x)} & 0 < x < 1, \\ 1 & x \ge 1 \end{cases} \qquad s(x) = \exp\left(-\frac{1}{(1+x)^2} - \frac{1}{(1-x)^2} \right)$$

Now, define the normalized radius

$$r = \frac{\rho}{\rho_0} = \frac{\sqrt{\xi_1^2 + \xi_2^2}}{|\boldsymbol{\xi}_0|}$$

Then, $W(\rho r) \neq 0$ in an annulus (*corona*) such that $\frac{2}{3}\rho_0 \leq r\rho_0 \leq \frac{5}{3}\rho_0$, localized with respect to the radial distance $\rho_0 = |\boldsymbol{\xi}_0|$ (Fig. 2a). Next, define

$$u = \sqrt{\gamma r} \cdot \left[\tan^{-1}\left(\frac{\xi_2}{\xi_1}\right) - \theta \right] = \sqrt{\gamma r} \cdot (\Theta - \theta), \qquad \gamma \in \mathbb{R}, \quad \theta \in [0, 2\pi]$$

Following the engineering convention θ is zero along the horizontal axis and positive counter-clockwise with respect to the horizontal. Then $V(\rho^{1/2}u) \neq 0$ if and only if $\rho_0^{1/2} |u| \leq \frac{2}{3}\rho_0^{1/2}$. This condition defines two parabolic fans with their apexes located at the origin $\xi = (0, 0)$ and their axis of symmetry inclined at an angle θ with respect to the ξ_1-axis (Fig. 2b). The aperture of these fans is scaled by the squared root of r and controlled by γ so that the larger is γ, the narrower become the lobes (Fig. 2b). Finally, define the function

$$\Phi(\boldsymbol{\xi}) = W(\rho r) \cdot V(\rho^{1/2}u) \cdot \exp\left(-i\langle \boldsymbol{\xi}, \boldsymbol{\Delta\xi} \rangle\right) \tag{6}$$

where the exponential factor allows for (unscaled) translation by $\boldsymbol{\Delta\xi} = [\Delta\xi_1 \ \Delta\xi_2]^{\mathrm{T}}$. It is evident that the support of Φ does *not* depend on the translation parameters.

Examples of this construct are shown in Fig. 3. Fig. 3a is a 3-D representation of a Φ centred on $\rho_0 = 0.1$ when the sampling rate is unity in both x_1 and x_2 directions and $\theta = 30°$, $\gamma = 8$. Fig. 3b illustrates the positive ξ_1 half-plane realization of four filters centred on $\rho_0 = 0.1$ but with different orientations

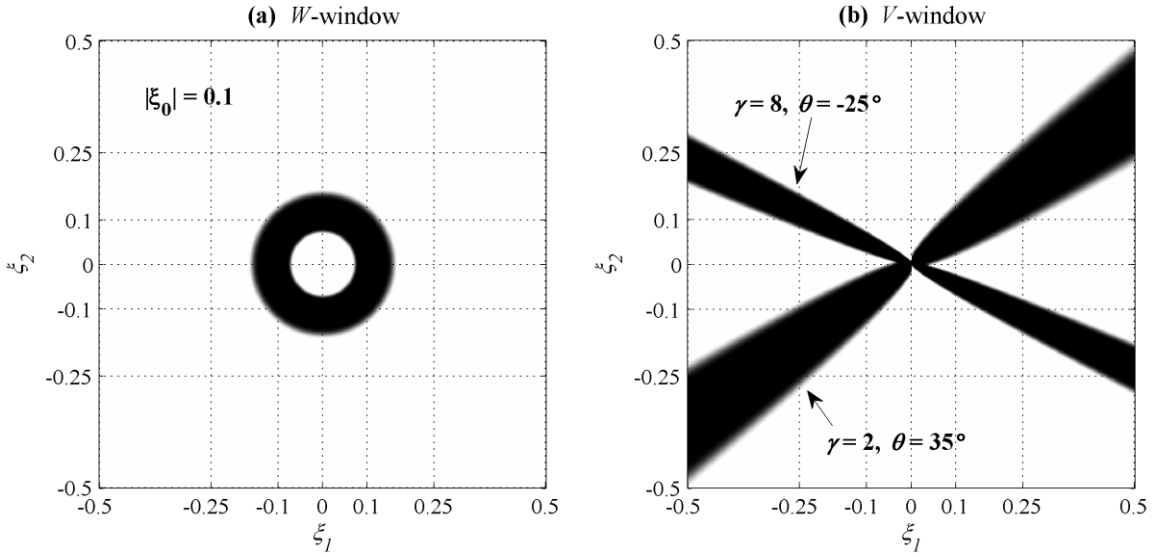

Figure 2: (a) Illustration of the $W(r)$ window when the sampling rate is unity in both x_1 and x_2 directions and $r = \rho/\rho_0 = \rho/0.1$. **(b)** Illustration of the $V(u)$ window when the sampling rate is unity in both x_1 and x_2 directions and $r = \rho/\rho_0 = \rho/0.1$ but for different anisotropy factors (γ) and azimuthal angles (θ).

and γ factors.

It is immediately apparent that γ controls the length to width ratio (aspect ratio) of Φ, which is a cardinal factor in its effectiveness as a filter: with increasing γ the width of Φ is shrinking so that for the same W, it becomes increasingly narrower. As a consequence, γ comprises a user-defined *anisotropy factor*. Fig. 3c illustrates the positive ξ_1 half-plane realization of four filters designed with different ρ_0 and azimuthal angles, but with the same anisotropy factor ($\gamma = 8$). For constant θ and γ, when $\rho_2 > \rho_1$ so that $r_2 = \rho/\rho_2$ and $r_1 = \rho/\rho_1$, $\Phi_2(\xi_2)$ is a dilated version of $\Phi_1(\xi_2)$.

As is apparent in Fig. 3b/ 3c, $\Phi(\xi)$ is defined on *polar wedges* with radial dimension (width) always $\rho_0\tilde{r}$, where $\tilde{r} :\Leftrightarrow \sup(r') - \inf(r') \Leftrightarrow \left\{r' \in [\frac{2}{3}, \frac{5}{3}] \supseteq r\right\}$, and azimuthal dimension (length) always

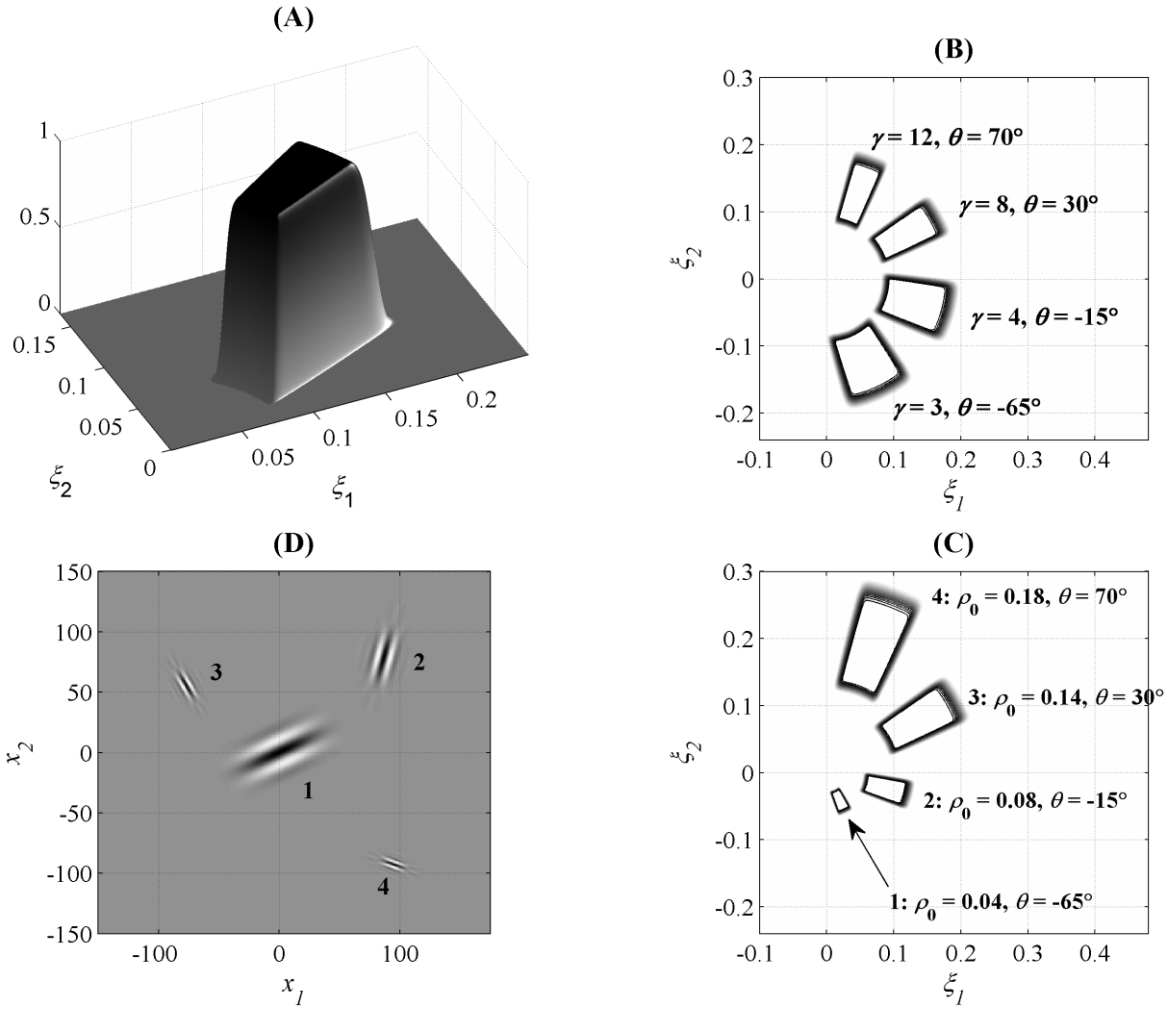

Figure 3: (a) Three-dimensional rendering of a ξ-domain curveletiform centred on $\rho_0 = 0.1$ and $\theta = 30°$, γ=8. **(b)** Positive ξ_1 half-plane realization of four curveletiforms centred on $\rho_0 = 0.1$ but with different azimuthal angles and anisotropy factors. **(c)** Positive ξ_1 half-plane realization of four curveletiforms with different foci ρ_0 and azimuthal angles but identical anisotropy factors. **(d)** The x-domain waveforms corresponding to the ξ-domain curveletiforms of Fig. 3c. In all four illustrations, the sampling rate is unity in both x_1 and x_2 directions of the x-domain.

$\rho_0^{1/2}\sqrt{\gamma\tilde{r}}$. Thus $\Phi(\boldsymbol{\xi})$ is supported in rectangles with dimensions related as *width* $\approx \gamma \times$ *length*^{2}, so that the proportionality factor between width and length squared is equal to the anisotropy factor. It follows that $\Phi(\boldsymbol{\xi})$ is exactly parabolically scaled when γ =1 and that any γ >1 *increases* the angular selectivity of $\Phi(\boldsymbol{\xi})$, hence angular resolution. Fig. 2d illustrates the x-domain waveforms $\varphi(\mathbf{x})$, corresponding to the ξ-domain $\Phi(\boldsymbol{\xi})$ filters of Fig. 3c, arbitrarily translated for the sake of visualization. Φ is anisotropic and by construction supported near its longitudinal axis but away from its transverse axis. It follows that $\varphi(\mathbf{x})$ will oscillate in the azimuthal direction of Φ and will be low-pass in the radial direction of Φ. Because these oscillation properties are preserved during translation, the x-domain waveform will always be enveloped by a ridge of effective width $(\rho_0 \tilde{r}\,)^{-1}$ and effective length $\rho_0^{-1/2}\left(\gamma\tilde{r}\right)^{-1/2}$ and will oscillate in a direction perpendicular to that ridge (see Fig. 3d), so that any γ >1 will increase the angular selectivity of $\varphi(\mathbf{x})$.

A direct comparison of Eq. (2) and Eq. (6) shows that Φ is essentially a curvelet but, as it happens, it is an *individual curvelet* that does not follow the scaling rules of the second dyadic decomposition – a maverick so to speak. It has *adjustable anisotropy* and is automatically localizable on any pair of coordinates in the ξ-plane. Accordingly, and in order to distinguish it from the definition of "curvelet" associated with the Curvelet Frame formalism, Φ is dubbed *"curveletiform*".

Due to the inherent similarity of curveletiforms and curvelets, the interaction of a Curveletiform Filter with C^2-continuous objects is identical to the interaction of curvelets with such objects. In the x-domain, when curveletiform and object intersect while aligned parallel to their longitudinal directions the transverse oscillatory part of the curveletiform will locally match the same-scale component of the object and will encode this information in the output. When curveletiform and object intersect at an arbitrary angle, the matching of the same-scale content will be partial and information will be lost to the curveletiform's low-pass longitudinal action. When the curveletiform and the object do not intersect, all information about the object is lost. Fig. 4 demonstrates these interactions. Specifically, Fig. 4a illustrates a contrived 512×512 data set featuring a wavy down-dipping set of intermittent reflections. In Fig. 4b the left panel illustrates the output of the ξ-domain curveletiform ρ_0 = 0.105, θ = 65° and γ = 8. The corresponding x-domain curveletiform has a slope of -25° and is almost perfectly aligned with the main trend of the "reflections" (Fig. 4a). In consequence, it extracts a clear and strong component of the signal. Conversely, Fig. 4c illustrates the output of the ξ-domain curveletiform ρ_0 = 0.105, θ = 55°, γ = 8. The x-domain curveletiform has a slope of -35° and intercepts the reflections at an angle of 10°; evidently, it cannot match a signal component of significant amplitude. Finally, Fig. 4d illustrates the output of the ξ-domain curveletiform ρ_0 = 0.056, θ = 65°, γ = 8. The associated x-domain curveletiform has correct slope but wrong scale: it extracts only a weak background process associated with the longer ξ-components of the data.

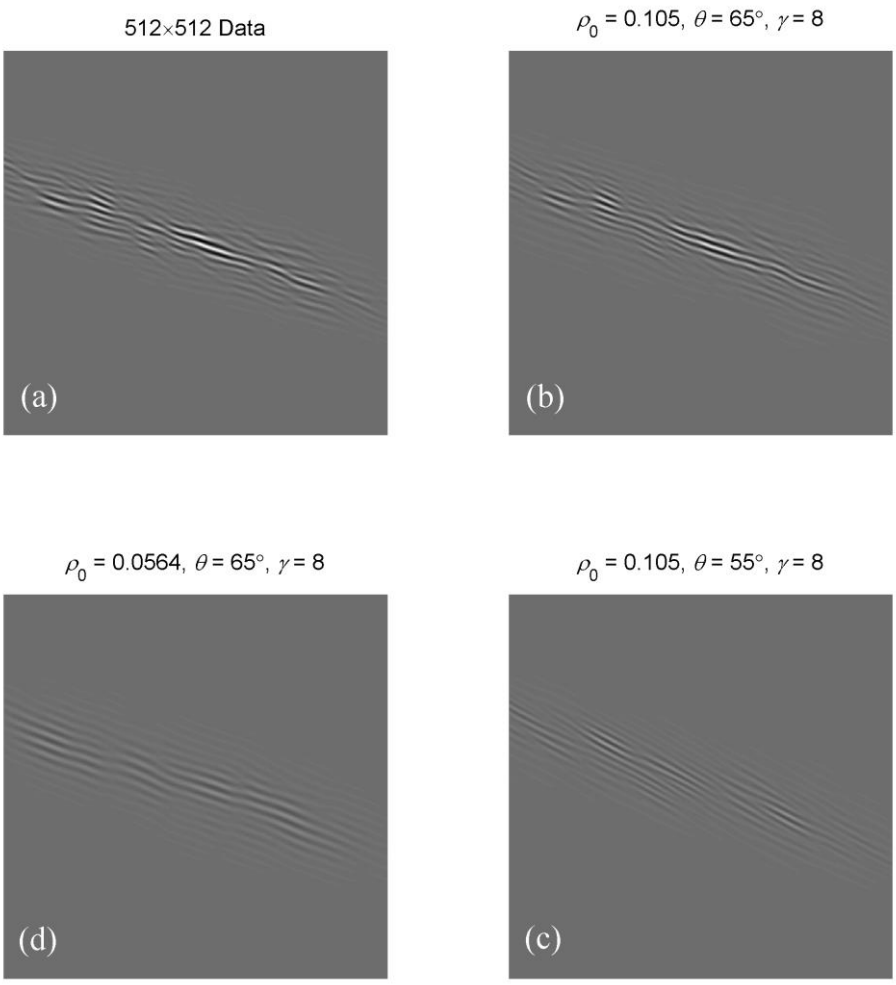

Figure 4: A demonstration of data and curveletiform interactions. **(a)** The data comprise a 512×512 matrix featuring only a set of wavy intermittent down-dipping reflections. **(b)** Reconstruction based on a ξ-domain curveletiform with parameters ρ_0 = 0.105, θ = 65°, γ = 8. **(c)** Reconstruction based on curveletiform with parameters ρ_0 = 0.105, θ = 55°, γ = 8. **(d)** Reconstruction based on curveletiform with parameters ρ_0 = 0.056, θ = 65°, γ = 8. In all four cases the sampling rate is unity in both x_1 and x_2 directions of the x-domain.

3. APPLICATION TO NOISY DATA WITH QUASI-STRAIGHT EDGES

It is now important to demonstrate the performance and capacity of a single-angle (single-dip) Curveletifom Filter (henceforth CF) in retrieving information from an image contaminated by high levels of noise and featuring straight edges. To this end, use will be made of a GPR data set containing straight dipping reflections from buried planar surfaces. This data has also been utilized in [10] and [34] in an analogous exposition of the performance of tuneable Directional Filters and the Curvelet Transform.

The data of Fig. 5a was collected with a monostatic GSSI SIR-2000 and 400MHz antenna. The radargram is shown as measured and comprises a 512 sample × 1024 traces section; the sampling rate is 0.1957ns and trace spacing is 0.01075m. The target of this demonstration is an up-dipping reflection

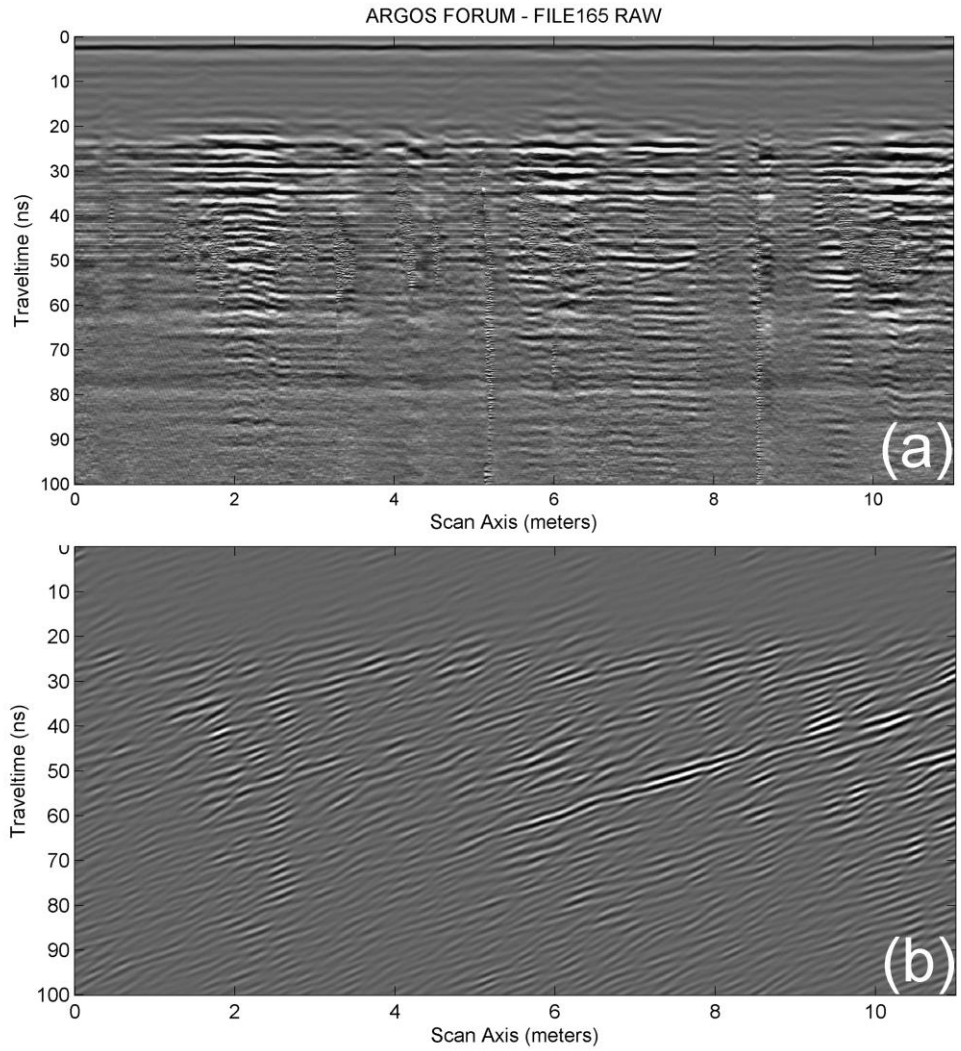

Figure 5: (a) B-scan radargram featuring an up-dipping linear reflector between ordinates 49–60ns and abscissae 6–7.8m, deeply buried in noise. The reflector may extend bilaterally to later times/shorter distances and earlier times/longer distances. **(b)** The same radargram after application of a CF with parameters ρ_0 = 0.09 θ = 165°, γ = 8 (data matrix coordinates).

which is clearly seen between coordinates (60ns, 6m) and (49ns, 7.8m) and may extend bilaterally to later times/shorter distances (approx. 66ns/5m) and earlier times/longer distances (approx. 37ns/10m). The data suffers from a hefty amount of noise which, after some straightforward analysis can be seen to comprise: a) Very low frequency isotropic interference at frequencies lower than 110 MHz and wavenumbers shorter than 1.9 m^{-1}; b) Mainly horizontal ringing with frequency lower than 210 MHz; c) High frequency bursts, spatially localized and mainly horizontal, with frequencies greater than 848 MHz; d) Broadband spatial variation of varying amplitude and vertical to sub-vertical orientation.

The design of a CF to extract the reflector is very simple. The main pulse of this reflection shows a positive – negative – positive polarity sequence and its duration can be measured at a few locations: the time between the positive peaks averages to 1.76ns. This is clearly an event rich in high frequencies – if it was a sinusoid, it would have a frequency of approx. 570 MHz. The width of the

pulse parallel to the scan line can be estimated to be in the range 0.19m to 0.32m, with an expectation value of 0.24m. This implies wavenumbers in the range 10.6m^{-1} to 6m^{-1} with an expectation value of 8.4m^{-1}. All that remains is to guess or estimate the dip and design a CF oriented at an angle perpendicular to that dip and localized with respect to an appropriate wavenumber.

At this point, it is important to emphasize that in order to properly implement the CF, it is recommended to treat the radargram as an image and carry out operation in *data matrix* coordinates and *not* in physical coordinates of wavenumber and frequency. In the opposite case, it would not be possible to define a unique ρ_0, representative of both frequency and wavenumber. In addition, the shape of the filter would be distorted meaning that it would no longer be a parabolically scaled wedge. The amount of distortion would depend on the ratio of the spatial to temporal sampling rates and would be different for different matrix dimensions, with outcome difficult to predict and even handle. In data matrix coordinates, the sampling rate is unity in both x_1 and x_2 axes and the Nyquist wavenumbers is 0.5 in both ξ_1 and ξ_2 axes. To define ρ_0 in data matrix coordinates, one may simply determine the target wavenumber k_0 in physical coordinates (by educated guess or direct measurement) and multiply it by the factor $0.5/K_j$, j=1,2 where K_j is the physical Nyquist wavenumber along the ξ_1 or ξ_2 axes. In the example treated herein, $K_1 = 1/(2\times 0.01075\text{m}) = 46.51\text{m}^{-1}$ and $k_0 \approx 8.4\text{m}^{-1}$ so that $\rho_0 \approx k_0 \times 0.5/K_1 \approx 0.09$ (dimensionless).

A brief note on the choice of a value for the anisotropy factor (γ) is also worthwhile. As indicated in Section 2.2, the magnitude of γ controls the angular selectivity of the curveletiform so that the larger it is, the finer the angular resolution. As there are no quantitative rules for assigning γ, in many applications direct experimentation guided by the specifications of angular resolution may be a useful approach. A long standing wisdom of (multi)directional filtering is that it generally pays to implement highly anisotropic filters, especially when single-orientation (or single-dip) features are to be isolated. In the case of CF, this points to using substantial anisotropy factors.

Fig. 5b illustrates the output of a CF with anisotropy factor $\gamma = 8$, oriented at $\theta = 65°$ and centred on the $\rho_0 = 0.09$ (expected wavenumber in data matrix coordinates). The dipping reflector stands out clearly and its continuity and lateral extent beyond the initially observable range is verified. It is also evident that the curveletiform has reconstructed parts of the reflection that have been previously missing of hidden. This is a result of its design and affinity to curvelets. As emphasized in Section 2.1, the microlocal properties allow any *recoverable* part of the data to be reconstructed with accuracy similar to the accuracy that would be feasible if the data was complete and noise-free [27, 31]. Because of their affinity to curvelets, curveletiforms (are understood to) share their microlocal properties and are thus as efficient in reconstructing missing or hidden data.

One very important point related to this example is the possibility of misconstruing for artefacts, certain elements of partially reconstructed data. Herein, the CF filter was used to perform a highly

anisotropic analysis of a specific reflector at a specific orientation: curveletiform and wavefronts were matched only along the orientations specified by the curveletiform, so that the partially reconstructed radargram contains almost uniformly dipping features, either localized or distributed at different locations. In general, if several small-scale such features appear distributed across a partially reconstructed radargram, they may (understandably) create a false impression of artefacts due to the filtering process. In reality, these are directionally filtered wavefronts or, more importantly, subtle data components not immediately evident to the "naked eye". A fine such example is the detection of a "hidden" reflector with geometrical characteristics identical to the main reflector's, located between (40ns, 1.3m) and (23ns, 4.2m). In the input data of Fig. 5a, this feature is heavily obscured and can be seen only after very careful inspection. In the filtered data, it forms a coherent dipping even for an extended part of the GPR section. This is neither coincidence nor artefact. It is the signature of a dipping interface with apparently weak reflectivity, obscured by interference of higher intensity data components and noise. It is successfully reconstructed and stands out due to the exceptional mirolocal properties of the CF. It is worth noting that the "hidden reflector" is for real as it can be observed with the same characteristics in neighbouring parallel sections.

The performance of the CF on this data set can be directly compared to corresponding results obtained by using the Curvelet Transform [34] and tuneable B-spline and Gabor directional filters [10]. Scrutiny will show that in this case (and presumably in analogous applications), the CF fares better than the CT because the localization of the filter is more flexible than what that attainable with then predefined partitioning scheme of the CT. The performance of the CF also compares very well, if not favourably, with that of the tuneable directional filters, with the added benefit that the CF is much easier to design and handle.

4. APPLICATION TO DATA WITH CURVED OBJECTS (EDGES)

In the general case, an image or radargram contains objects with singularities on curves, as for example curved edges or variable-dip reflections from single or multiple reflectors. A singularly oriented CF will extract only part of the available orientation-dependent information because it is highly selective. If, however, one wishes to extract scale-dependent information over a range of orientations, one may combine partial images obtained by application of the same filter rotated to different directions. The specific method of partial image combination used herein has been proposed by [8] and borrows insight from techniques commonly used in edge and contour detection. Letting **D** denote the Fourier transform of the data, the procedure entails the application of the CF fixed on a given $|\xi_0|$ but computed over a sequence of angles $\theta_1,\ldots,\theta_N$ over an arc $\theta_1\theta_N$. This will yield a series $n = 1, \ldots N$ of outputs $\hat{\mathbf{D}}_n(\theta_n,\rho_0)=\langle \mathbf{D},\mathbf{\Phi}(\theta_n,\rho_0)\rangle$ that can be stacked in the weighted least-squares sense as

$$\bar{\mathbf{D}}(\theta_1:\theta_N,\rho_0)=\sum_{n=1}^{M}\hat{\mathbf{D}}_n(\theta_n,\rho_0)w(\theta_n,\rho_0)\Big/\sum_{n=1}^{N}w(\theta_n,\rho_0)$$

The stacking weights implemented herein are generally functions of a measure of the energy contained in the output data normalized by the same measure of the energy contained in the input data in the sense:

$$w(\theta_m,\rho_0)=\left\|\hat{\mathbf{D}}(\theta_m,\rho_0)\right\|_n\cdot\|\mathbf{D}\|_n^{-1},$$

where n can be 1 (Manhattan norm), 2 (Euclidean norm), or ∞ (infinity norm). It is also possible to set $w(\theta_m,\rho_0)=1$, (i.e. obtain a straight arithmetic average of the outputs at different rotation angles). This weighting scheme guarantees that the final output will not be disproportionally dominated by powerful spectral components and that it will be a faithful representation of the information originally contained in the input data.

This filtering scheme facilitates the combination of "partial", same-scale/ variable-dip data subsets into a scale-dependent but dip-independent image and may account for any variation in the angle of dip, including the case of (smoothly or sharply) curved interfaces. Moreover, the stacking will tend to smear dip-dependent noise features eluding the filter at a given temporal or spatial scale, further enhancing the S/N ratio.

4.1. Example 1: Edge detection according to scale in a photographic image.

In order to demonstrate how this process works, it will first be applied to a photographic image with complex albeit easily and intuitively recognizable characteristics. Fig. 6 introduces the ERTman, a geophysicist caught in somewhat lazy action during an ERT survey in a suburban environment. The ERTman image comprises a 1632×1224 real matrix and exhibits high and low contrasts as well as curved and straight "interfaces". The former include the contrast between the ERTman's jacket and the background, discoloration lines on the jacket and several shadows cast on the walls of the background buildings. The latter set includes shades on the white rope rolls held under his arms, as well as between the wires and caps of the electrode connectors around his neck. There are also fuzzy traits (e.g., the canopy of the three in the background, the ERTman's beard) and fuzzy contrasts (e.g. the ERTman's hair against the canopy and his beard against his face). The image also includes fine spatial details, with particular reference to the springs of the electrode connectors and the grating of the closed window at the far background.

Noting that for general images the Nyquist wavenumber is 0.5 so that $\rho_0 \equiv k_0$, and that the desired k_0 can be predefined or determined by direct measurement, (as in the example of Section 3), Fig. 7 illustrates the output of different filters applied to the ERTman image as follows: Fig. 7a illustrates the output image $\bar{\mathbf{D}}(\theta_1:\theta_N,\rho_0)$ for ρ_0 = 0.089, γ = 20 and $\theta \in$ [-90°, 90°], sweeping the arc in steps of

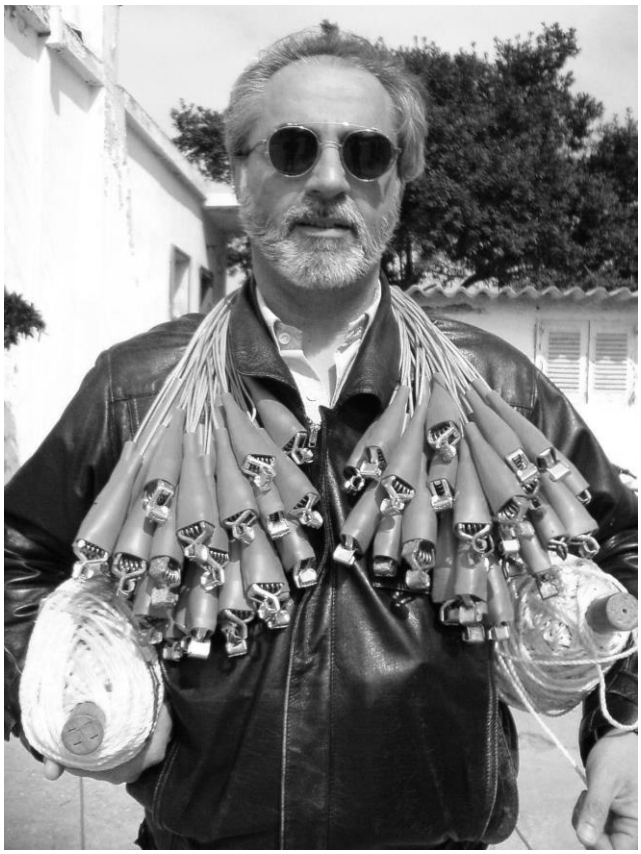

Figure 6: The ERTman image. See text for details.

10°. Fig. 7b is the same but only displayed after thresholding subject to the condition $\bar{\mathbf{D}}_{i,j} > \sigma$, where σ is the standard deviation of all elements of $\bar{\mathbf{D}}$. Fig. 7c is as per Fig. 7a but for ρ_0 = 0.178 and Fig. 7d is the corresponding thresholded image. Thus images 7a/ 7b are of coarser scale (shorter wavenumber) and images 7c/ 7d or considerably finer scale (longer wavenumber).

It is evident that the two filter designs function as edge detectors that extract information at different levels of detail (different scales). It is probably not advisable to proceed with a detailed description of the results within the context of this presentation and is up to the reader to make specific observations and comparisons. It is possible, however, to point out some general features of the results. Thus, all the (straight and curved) linear high and medium contrast interfaces have been successfully discriminated in all outputs. However, the resolution of the low-contrast and/or finer size interfaces is associated with the scale. Accordingly:

a. The fine interfaces between the wires of the electrode connectors are only approximately resolved in the coarser scale output (Fig. 7a/ 7b), but they are fully discriminated to the level of individual wires in the finer scale output (Fig. 7c/ 7d).

b. The low-contrast/ fine-scale interfaces between the caps of the electrode connectors are generally resolved, with particular reference to Fig. 7c/ 7d.

c. All the clips of the electrode connectors are successfully discriminated and in the coarser scale the winding of their springs is discriminated as well.

d. In Fig. 7a/ 7b, only the perimeter of the ERTman's shades is outlined. Conversely, in Fig. 7c/ 7d the entire frame is resolved in detail.

e. The fuzzy regions in ERTman image are also associated with scale: For instance only the larger dark-shaded regions (sub-structures) of the tree canopy are outlined in Fig. F7a/ 7b whereas many details are picked up in the finer scale image. The very fuzzy and low-contrast interface between the ERTman's hair and the canopy (as well as internal shadings in the hair) is not resolved in the coarser

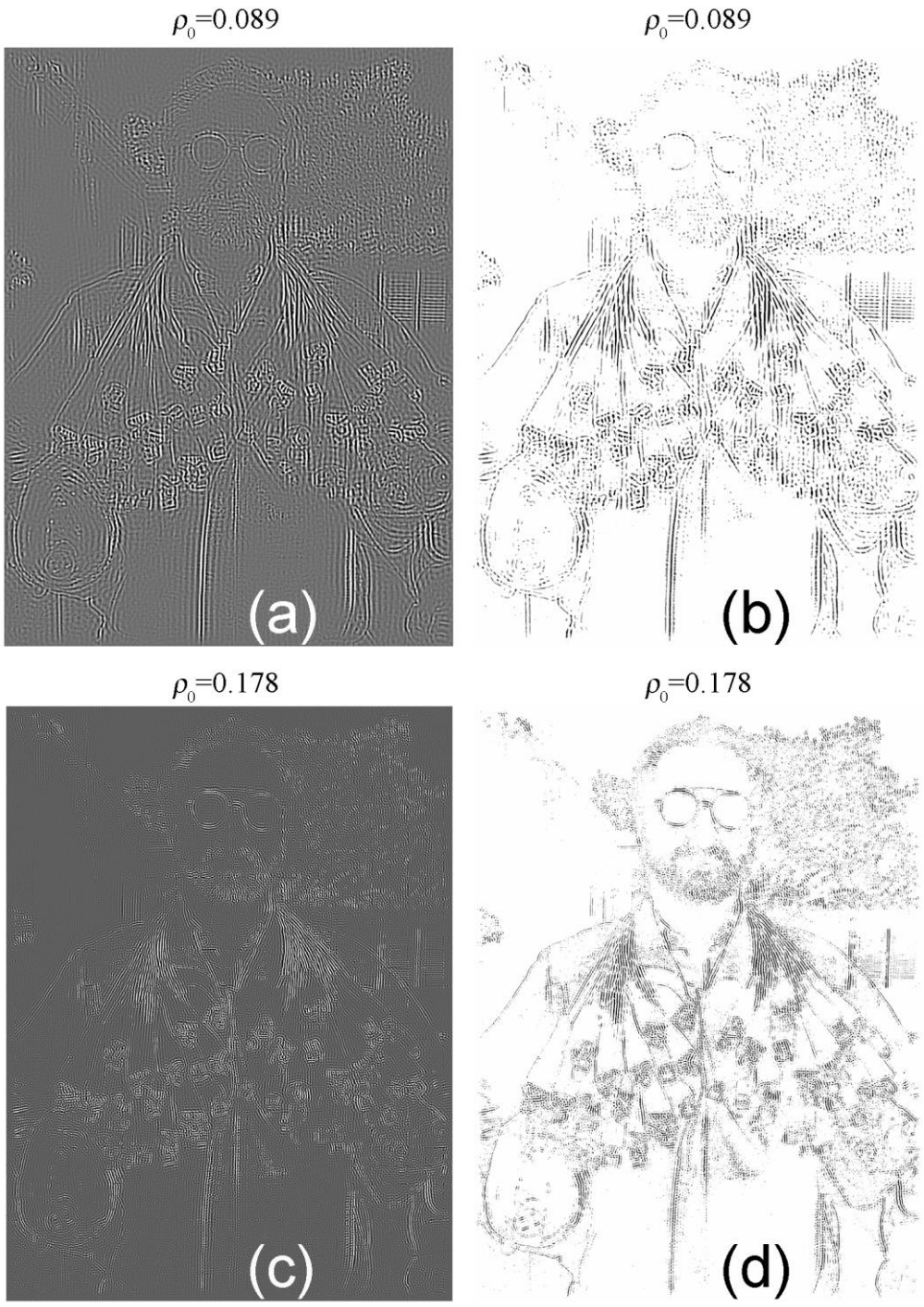

Figure 7: (a) The ERTman image after application of a CF centred on ρ_0 = 0.089 m^{-1}, with γ = 20 and $\theta \in$ [-90°, 90°], sweeping the arc in steps of 10°. **(b)** The image of Fig. 7a after thresholding values lower that one standard deviation (see text for details). **(c)** The ERTman image after application of a CF centred on ρ_0 = 0.178 m^{-1}, with γ = 20 and $\theta \in$ [-90°, 90°], sweeping the arc in steps of 10°. **(d)** The image of Fig. 7c after thresholding values lower that one standard deviation.

scale and only marginally discriminated in the finer scale. Conversely, the internal texture of the hair and the beard is particularly well resolved in the finer scale (Fig. 7c/ 7d).

It is interesting (and significant) to observe that along interfaces such as the black ERTman's jacket and be white background wall, where the contrast is very high and localized, assuming the character of

Figure 8: Photographs of the fragmented limestone setting in which the data of Scans 61 and 86 was recorded. Void or laterite-filled faults and joints can clearly be observed. Images are courtesy of Mr P. Sotiropoulos, Terra-Marine Ltd., Greece (http://terra-marine.gr).

a step function, the output exhibits low-amplitude spurious oscillation. A step-like function is associated with a very broadband spectrum that is *not* characterized by any particular scale. The application of the CF and its narrow-band passing action results in incomplete (partial) reconstruction of the step function, as it admits only wavenumbers matching the filters characteristics: the incomplete reconstruction generates the spurious oscillation. Similar effects can be observed in analogous narrow-band operations on very broadband events as has also been pointed out in [34]. Although the problem of spurious oscillation should hardly be an issue with real GPR data[1], it is always advisable to exercise caution when using the CF on broadband (e.g. transient) features. At any rate, thresholding the output appears to take care of this problem.

4.2. Example 2: Fracture detection in 2-D GPR data.

The first example to be shown herein uses a complex data set with moderate S/N ratio to demonstrate the performance of multidirectional curveletiform filtering in the detection and extraction of localized, quasi-linear reflections from faults and fractures. Fig. 9a illustrates a radargram collected with a Måla GPR system and 250MHz antenna. The data was measured on a levelled surface above massive limestone fragmented by (now inactive) conjugate normal faulting and jointing; karstification has nucleated along the fault walls and many of the resulting voids were subsequently filled with ferriferous argillaceous material of lateritic composition (Fig. 8).

[1] This would require reflection events with step function characteristics which are rather impossible, or very energetic, very sharp (delta-function) pulses that are rather unlikely in dispersive, real-world materials.

The data, henceforth to be referred to as "Scan 61", is shown after pre-processing with time-zero adjustment, global background removal, amplification with the "inverse amplitude decay" technique [39] and resampling to a 1024 sample × 1024 trace matrix (the sampling rate is 0.1909 ns and trace spacing 0.0256 m). Noise is not a significant problem with the exception of some peculiar, interference of unknown origin, intermediate strength and "checkerboard" spatio-temporal characteristics appearing at different locations of the radargram. It is straightforward to observe linear and quasi-linear reflections that can be attributed to planar or quasi-planar interfaces created by faulting and fracturing. It is also straightforward to recognize that the apexes of some of these features are decorated with hyperboloid textures, meaning that they are associated with diffraction fronts that mask their true length and location. Accordingly, the data was migrated assuming a uniform velocity

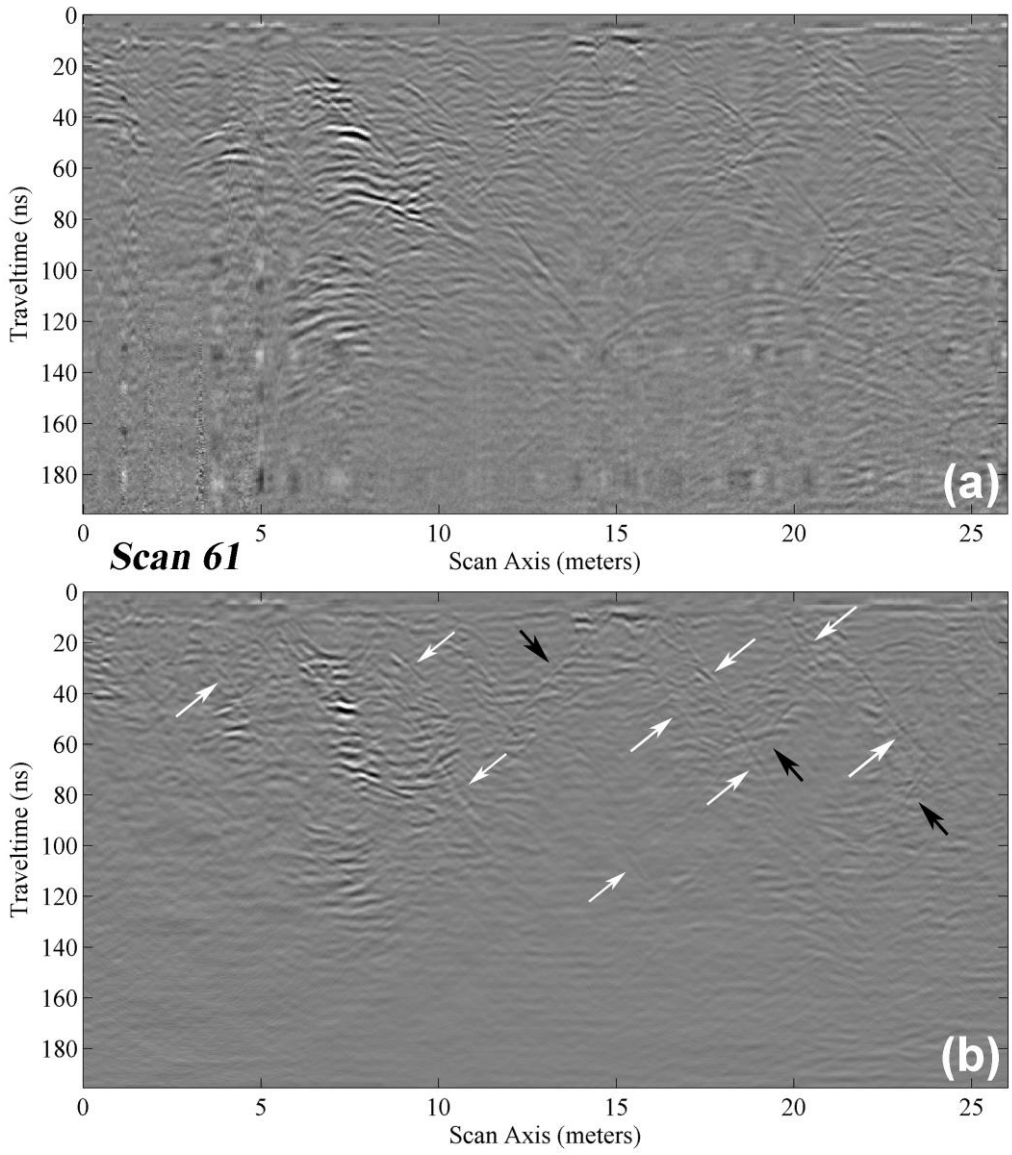

Figure 9: (a) A B-scan radargram codenamed Scan 61 and measured above massive fragmented limestone. The data has been pre-processed as detailed in the text and is used courtesy of Mr P. Sotiropoulos, Terra-Marine Ltd (http://terra-marine.gr). **(b)** The data of Scan 61 migrated with a uniform velocity of 0.085 m/ns. Black and white arrows point to linear reflections which are discernible but very faint in the radargram.

of 0.085 m/ns, estimated by fitting diffraction front hyperbolae observed elsewhere in the study area. The migrated section is shown in Fig. 9b where it is apparent that the checkerboard noise has been smeared out by the migration, leaving a very low frequency/ wavenumber background.

The main features observable in the migrated section are: (a) Down-dipping reflections attributed to faults and fractures, with examples pointed to by white arrows. (b) *Very* faint, up-dipping quasi-linear

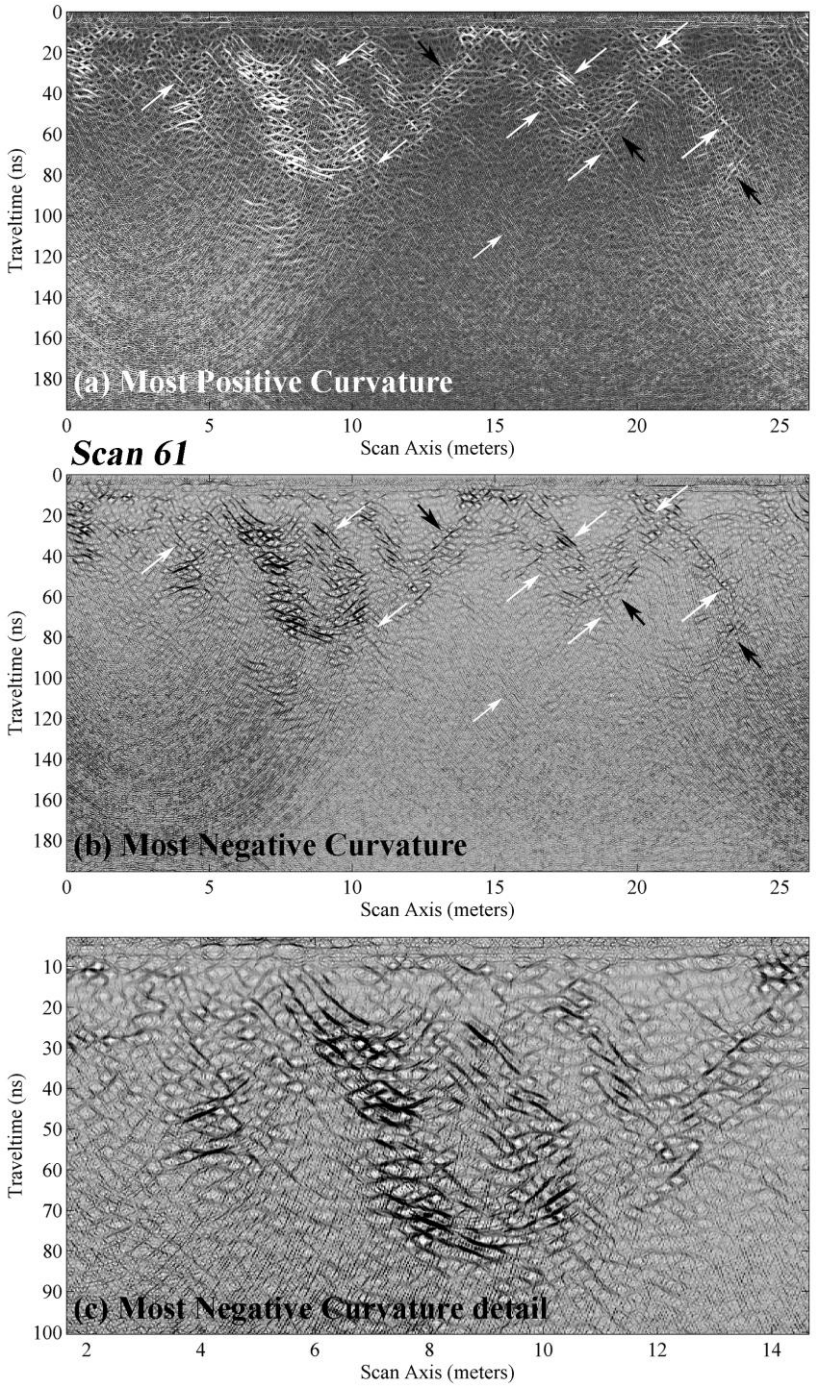

Figure 10: (a) The most positive curvature attribute computed from the migrated Scan 61 (Fig. 9b). **(b)** The most negative curvature attribute computed from the migrated Scan 61 **(c)** Detail of the most negative curvature image. In all cases the black and white arrows are positioned identically as per Fig. 9b.

reflections also attributed to fractures with examples pointed to by black arrows. (c) Clusters of strong reflections along the larger fracture zones, (e.g. between 5–10m and 40–80ns), sometimes associated with the intersection of down- and up-dipping fractures. The apparent spatial widths of the quasi-linear reflections can be measured on the radargram to be 0.2 – 0.4 m, so that their expected wavenumbers would be 2.5–5 m^{-1}. Their apparent dip can also be measured and *in data matrix coordinates* ranges between 65° and 75° for the down-dipping, and between −75° and −60° for the up-dipping reflections.

The interpretation of the migrated Scan 61 will be supported with imaging and analysis of most positive and most negative curvatures, which are curvature attributes successfully used for fault detection in 3-D seismics (for comprehensive introductions to the concept of curvature attribute see [40, 41] and references therein). The extrinsic curvature of a surface can be defined as the rate of change of the angle through which the tangent to a surface turns while moving along a curve on the surface, or even more naïvely, how fast the surface bends. By convention, the curvature at a point on a surface is positive when vectors normal to the surface diverge in the vicinity of that point, i.e. when the shape of the surface is convex as in hills, ridges etc. Conversely, the curvature is negative when vectors normal to the surface diverge in the vicinity of a point, i.e. when the surface is concave as in valleys. Out of the infinity of possible curves and corresponding curvatures on a three-dimensional surface, the most useful subset is the one defined by curves in the directions of the normals to the surface. The curvatures of such curves are called *normal*. The *most positive curvature* K_+ at a point on a surface is the largest of all positive values determined from all possible normal curvatures at that point. Likewise, the *most negative curvature* K_- is the smallest of all negative values determined from all negative normal curvatures. By mapping the most positive and negative attributes one obtains edge-type images in which lineaments of high K_+ values trace ridges and lineaments of low K_- values trace valleys and troughs in the texture of the data. What is important to clarify in this necessarily parsimonious introduction, is that in geological settings analogous to that of the present example, the most positive and negative curvature attributes derived from GPR data can be used to identify fragmentation down to the level of individual rock blocks, because these would be delimited by the ridges and troughs of reflections from their interfaces with neighbouring blocks, provided of course that said interfaces are sufficiently reflective.

Fig. 10 illustrates the most positive and most negative curvatures of the migrated Scan 61, computed with a method outlined in [40]. Both the most positive (Fig. 10a) and most negative (Fig. 10b/ 10c) curvatures exhibit alignments corresponding to quasi-linear reflections observable in Fig. 9b. At distances 5–11 m and traveltimes 20–80 ns, the rock appears to be heavily fragmented and brecciated; as can be seen in the enlarged image of Fig. 10c, it comprises a mosaic of blocks whose outlines and orientations are clearly associated with the purported up- and down-dipping fractures. The heavy apparent fragmentation indicates that this area may correspond to a down-dipping fault zone. At distances beyond 15m "fragmentation" is less intense but still present within and immediately around

the purported fractures. As is also evident in Fig. 10, the quality of estimation deteriorates sharply with increasing noise, so that curvature attributes cannot yield reliable information at traveltimes longer than 80ns, even in areas where structure is definitely discernible to the "naked eye". This is the domain where the CF is expected to perform superiorly.

The expected wavenumbers and apparent dips of the quasi-linear reflections indicate the design parameters of the CF. Accordingly, the target wavenumber was set to 3m^{-1} in physical coordinates which translates to $\rho_0 = 0.0767$ in data matrix coordinates ($K_1 = 1/(2\times0.256)$, $\rho_0 \approx 3 \times 0.5/K_1 \approx 0.0767$, also see Section 3). The anisotropy should also be very high so as to favour quasi-linear features through increased angular resolution; accordingly, γ was assigned a value of ~~$\gamma =$~~ 40. Finally, the observed apparent dips define the arc over which to apply the filter. Thus, θ should vary in the interval [–40°, –20°] for synthetic, and in the interval [10°, 35°] for antithetic fractures. Fig. 11 illustrates the output of a multidirectional application of the CF over the arcs [-40°, -20°] $\cup$ [10°, 35°] in steps of 2.5°. The top panel displays the actual output of the filter, the middle panel the output after thresholding for all values $\bar{\mathbf{D}}_{i,j} < \frac{5}{4}\sigma$ and the bottom panel displays the thresholded output in natural scale after depth migration.

It is straightforward to see that albeit very weak and practically obscured by other components, up-dipping reflections have generally been successfully detected, even at locations at which it was previously not possible to observe with "naked eyes", or were too noisy to yield distinguishable alignments of curvature attributes: such an area is located at distances 5–10 m and traveltimes 80–150 ns. Between zero and 14 metres the concentration and geometry of linear reflections from purported fractures is such that, in association with the "fragmentation" observed in the curvature attributes, clarifies that the measurements straddle a down-dipping fault zone which facilitated water percolation, karstification and subsequent deposition of lateritic material. This process is thought to generate the strong reflections observed between 6 and 10 metres in the radargram (Fig. 9). At distances longer than 12m the rock, albeit fractured, is considerably healthier. The angle between the up- and down-dipping fractures is approx. 60°, (Fig. 11-bottom), indicating that they form a conjugate set. The kinematics of the faulting process can also be assessed. For instance, the up-dipping reflections turn out to be faults that dislocate the down-dipping fractures in a right-lateral sense (e.g. see Fig. 11 at distances 15-24m, traveltime intervals 16-80 ns and depth ranges 0.1 – 4m). The down-dipping faults also appear to dislocate the up-dipping faults in a left-lateral sense (e.g. see Fig. 10 at distances 11-15m, traveltimes 5-65ns, depths 0.1 – 2.5m). This indicates a system of low-angle *synthetic* up-dipping, and high-angle *antithetic* (down-dipping) faults, developing in an apparently extensional local stress regime.

The second example comprises a complex data set with high S/N ratio, measured near Scan 61 and will be referred to as "Scan 86". The radargram is displayed in Fig. 12a after pre-processing with time-

zero adjustment, global background removal, amplification with "inverse amplitude decay" [39], resampling to a 512 sample × 1024 trace matrix (sampling rate 0.382 ns, trace spacing 0.033 m), wow elimination, f-k migration and depth migration, both with a velocity of 0.085m/ns. A natural (1:1) aspect ratio is used in this, and all other displays of Fig. 12. Fig. 12b illustrates the most negative curvature computed from the pre-processed data of Fig. 12a.

In both Fig. 12a and 12b, it is possible to observe strong, quasi-linear, up-dipping reflections and most negative curvature lineaments with apparent dips –50° to –45°, as well as faint, quasi-linear, down-

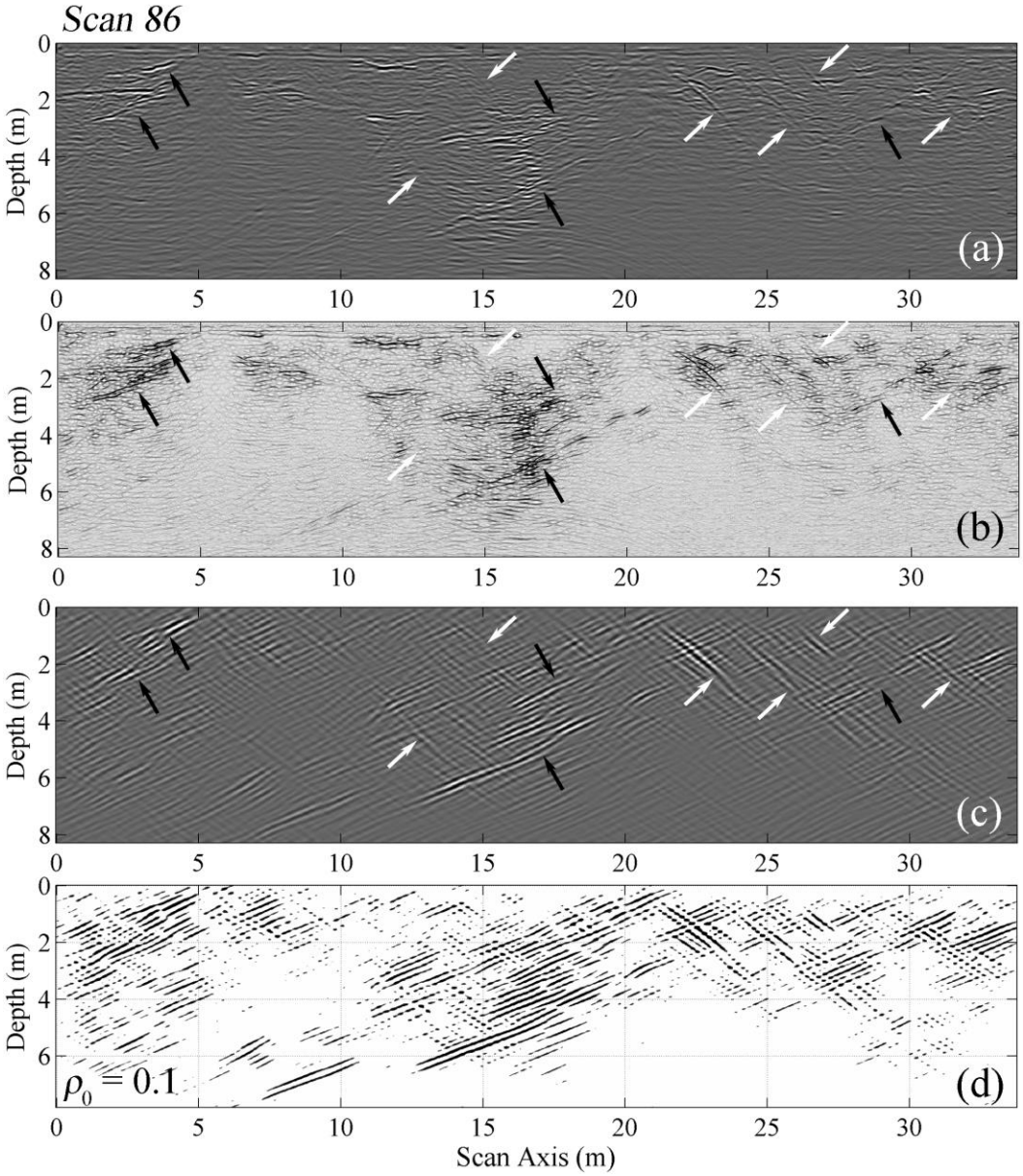

Figure 12: (a) A B-scan radargram codenamed Scan 86 and measured above massive fragmented limestone. Black and white arrows point to (conspicuous or faint) quasi-linear reflections. The data has been pre-processed and depth migrated as detailed in the text; it used courtesy of Mr P. Sotiropoulos. **(b)** The most negative curvature associated with Scan 86. **(c)** Scan 86 after multidirectional application of a CF with parameters $\rho_0 = 0.1$, $\gamma = 40$, $\theta \in [-40°, -10°] \cup [20°, 50°]$. The black and white arrows are positioned identically as per Fig. 12a/ 12b. **(d)** As in (c) but thresholded for values lower than $5\sigma/4$.

dipping reflections/lineaments with apparent dips 60° to 70° (all in data matrix coordinates). Following the interpretation given for Scan 61, the former can be attributed to synthetic, and the latter to antithetic fracturing and faulting. Some of the more conspicuous such features are indicated with black (up-dipping/synthetic) and white arrows (down-dipping/ antithetic). Moreover, the apparent spatial widths of the quasi-linear reflections can be estimated on the radargram to be 0.2–0.4 m, so that their expected wavenumbers would be 2.5–5 m^{-1}, in manifest consistence with corresponding measurements made in Scan 61. In Fig. 12a, a cluster of very strong reflections can also be observed at distances 15 – 18m and depths 3-7m, distributed almost along the vertical. As indicated by the most negative curvature in Fig. 12b, this area is highly disturbed and should be intensely fragmented. Furthermore, it appears to extend between two rather conspicuous up-dipping reflections. One plausible explanation for the quasi-vertical distribution of the disturbance is the existence of karstification effects developing in the brecciated zone between the walls of a synthetic fault. Significant disturbance (fragmentation) also appears to exist at depths 0 – 4m and distances 1 – 4 m and 22 – 35 m respectively.

As before, the design parameters of the CF are determined by the expected wavenumbers and apparent dips of the quasi-linear reflections. The target wavenumber was set to 3.1m^{-1} in physical coordinates, which translates to $\rho_0 \cong 0.1$ in data matrix coordinates. The aspect ratio γ was also set to 40 so as favour linear features. Finally, θ was allowed to vary in the interval [-40°, -10°] $\cup$ [20°, 50°] in steps of 2.5°. Fig. 12c illustrates the actual output of the filter and Fig. 12d the same after thresholding for all values lower than $5\sigma/4$. The area between 7 and 25 m is characterized by a cluster of strong up-dipping reflections which can now be attributed to a local synthetic fault. The upper fault wall is indicated by a cluster of tightly spaced reflections located at distances 10–21m and depths 4–0m. The lower fault wall is delimited by strong reflections at distances 7–25 m and depths 8–3m. The total aperture of the fault appears to be 3 – 4m. It is straightforward to observe a very high density of parallel up-dipping reflections (presumably from synthetic fractures) in the highly disturbed area between 15–18m distance and 3-7m depth, which is now clearly seen to develop in the brecciated zone between the fault walls. The up-dipping reflections are all strong and dwarf those from local antithetic fractures; notably, their presence (and lateral extent) was mostly *hidden* in the input radargram (Fig. 12a). It is also apparent that the density of up- and down-dipping reflections is high in the other areas of suspected fragmentation, (depth 0–4m, distances 1–4 m and 22–35 m respectively), signifying the presence of smaller scale synthetic and antithetic faults and unhealthy native rock condition. It may be concluded that as with Scan 61, the application of the CF to Scan 86 provides an informative profile of the geological and geotechnical condition of the situation conditions under the scan line.

To conclude this section, Fig. 13 illustrates the (multidirectional) application of the CF to five parallel B-scans (86 – 90), with Scan 86 (reference) shown at the bottom. All data has been treated as detailed above for Scan 86. It is rather straightforward to observe that the synthetic (up-dipping) fault identified

in Scan 86 can also be identified in all five sections and that its location shifts to the right by as much as 5 m between Scans 86 and 90. It is also apparent that fracture density (hence damage) varies along strike and as per Scan 86, it is always higher in rock volumes associated with fracture intersection and secondary effects, such as karstification.

Notable also is a persistent volume of damaged rock between 0 and 5 metres at the left of all scans, the changing distribution of damage in the first four metres of depth and the changing geometry of the

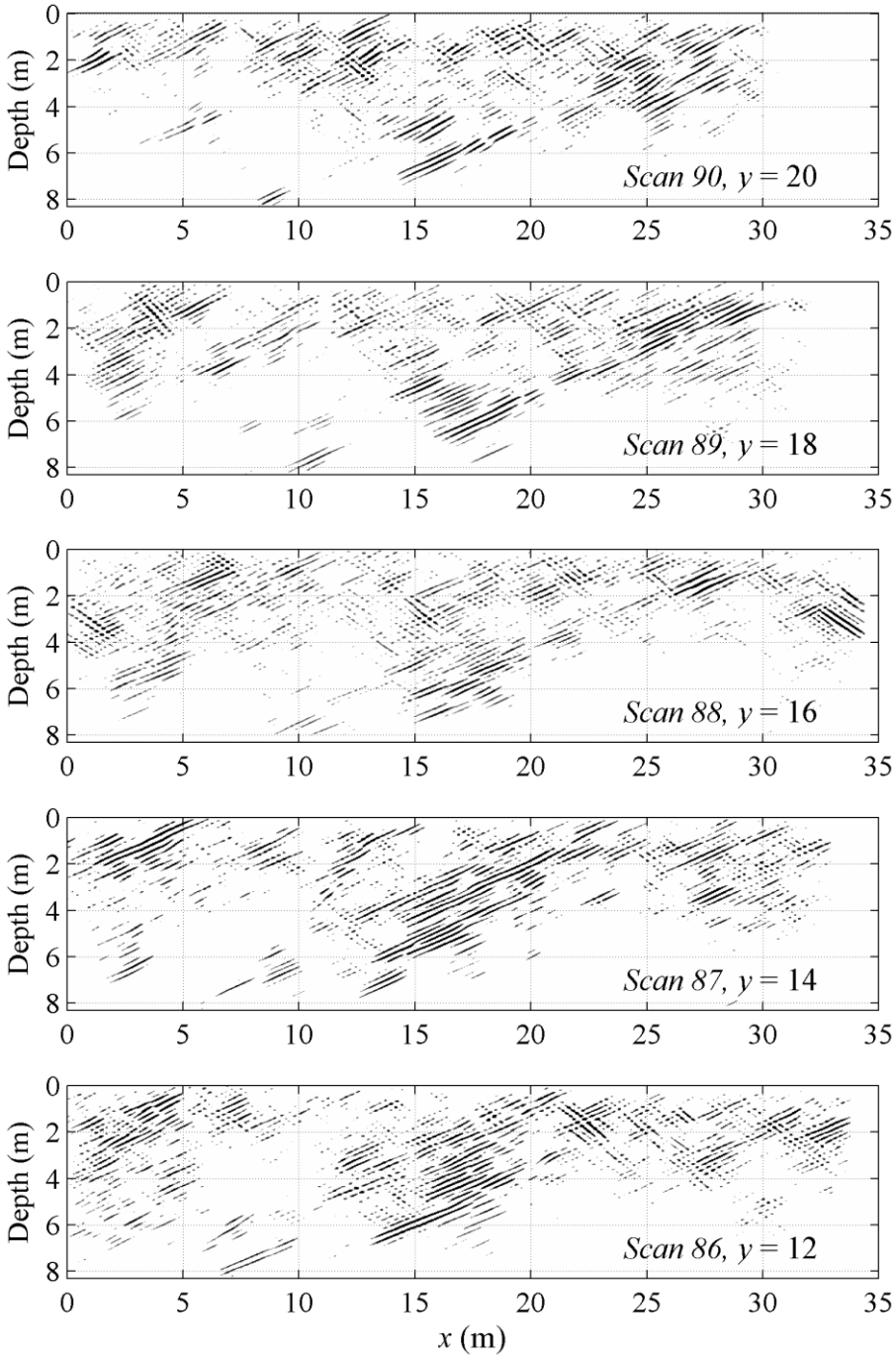

Figure 13: Multidirectional application of the CF to five parallel B-scans (86 - 90. All data has been treated as detailed in the text for Scan 86, which is shown at the bottom. Filter outputs are displayed after thresholding for values lower than $5\sigma/4$.

interface between damaged (high fracture density) and healthier rock (low fracture density). As a concluding general observation, this type of fracture imaging appears to provide an informative picture of the geotechnical conditions of the survey area.

5. DISCUSSION AND CONCLUSIONS

The present work introduces a directional filtering technique based on the design and properties of curvelets and discusses its application to the retrieval of geometrical information from digital images, although herein emphasis is placed on the detection of fractures with B-scan GPR data. The technique is simple to implement, computationally inexpensive and appears to be powerful: even without a priori information, with some straightforward experimentation (trial and error) the analyst may retrieve information about any resolvable structural scale at any orientation, sometimes with surgical precision.

The filter is essentially a curvelet that can be tuned (centred) on specific wavenumbers, so called *target wavenumbers*. This is done simply by normalizing the physical wavenumber spectrum by the target wavenumber, so as to shift the filter's support at the location of the target. This offers increased simplicity and flexibility because the filter can then be automatically constructed by using an orthogonal wavelet basis (radial and azimuthal Meyer windows are used herein) and does not require the definition of shaping parameters other than one which controls its anisotropy, hence angular resolution. While it retains the design characteristics and microlocal properties of curvelets, the filter is not bound to the scaling rules of the second dyadic decomposition employed in the curvelet transform but is automatically localizable and scalable (tuneable) around any pair of coordinates in the Fourier plane, hence any orientation-dependent trait in the data. The filter is a "maverick" curvelet that does not conform to the Curvelet Frame formalism, hence it is dubbed *Curveletiform Filter* (CF).

The CF can be used in single- or multi-directional mode. A single-directional (single-dip) CF will extract only part of the available orientation-dependent information because it is highly selective. If, however, one wishes to extract same-scale information over a range of orientations or dips, it is possible to combine partial images obtained by application of the same filter rotated to different directions so as to account for any variation in the orientation or dip. Accordingly, the filter can be used to retrieve curved features of specific scale and geometry for further analysis. In geotechnical applications of GPR (and seismics) this would entail, for instance, identification of waveforms from faults and fractures, discrimination of signals from small and large aperture fractures and faults, different phases of fracturing and faulting etc. More importantly, owing to its kindred with curvelets, the CF can retrieve any *recoverable* piece of information even if the data is generated by complex structures and immersed in noise, with accuracy similar to the accuracy that would be feasible if the data was complete and noise-free.

The merits of the CF are apparent but, as with all methods, there are caveats. As [34] has also pointed out, the application a highly localized filter (narrow-band operation) to broadband events that are not characterized by particular scales (e.g. transient wavefronts), may result in low amplitude spurious oscillation due to incomplete partial reconstruction. It is therefore necessary to have this in mind when dealing with data exhibiting step-function discontinuities, very narrow delta impulses or analogous such broadband characteristics. At any rate, thresholding the output appears to be a simple means of circumnavigating the problem.

A possibly more serious issue is the risk of misinterpreting the output in terms of artefacts. For example, when variable-geometry objects exist in the image or data and a highly anisotropic analysis is performed, (e.g. when single-angle geometrical information is required), the curveletiforms and the objects will be matched only along the orientations specified by the curveletiforms. Depending on the distribution of the objects, uniformly oriented localized features, or alignments of features may appear at different places in the output image. In most cases these are subtle data components that are not immediately apparent to the observer and can be misconstrued for artefacts. A fine such example can be studied in Section 3. Accordingly, caution is needed so as not to dismiss a valid output.

A final important question is the existence of other analysis methods that can provide similar or even improved efficiency. The answer is affirmative albeit not simple. The CF is, in effect, a straightforward f-k filtering technique and in some cases with simple data and/or noise structures, conventional procedures (e.g. f-k filters) may perform equally well. However, conventional f-k filtering may become impractical with increasing data complexity. Some advanced orientation-sensitive *X*-let transforms may also offer efficient alternatives, as for instance those optimized for the processing of edges (shearlets, riplets and contourlets). When the data is strongly oscillatory, designs optimized to process oscillating textures (e.g. wave atoms) may be superior because "*curvelets only capture the coherence of the pattern along the oscillations, not across*" [25]. Adaptive low-dimensional approximations (e.g. wedgelets) and adaptive orthogonal expansions (e.g. bandlets) may perform efficient approximations of objects with geometric singularities, although such objects are generally not common in GPR data. The list is certainly long and cannot be exhausted herein, to anyone's satisfaction.

With respect to GPR data and to the best of the Author's knowledge, there are only three other methods designed to retrieve geometrical information. The first is a parametric local-dip image decomposition approach that utilizes Local Radon Transforms [42, 43]. The method has been claimed to be robust and efficient in the recovery of coherent dipping features; it has also been suggested [42] that it can be used to remove coherent and random noise, separate wavefields and reconstruct missing data. Unfortunately, its overall performance cannot be effectively assessed for lack of published results. Moreover, the method cannot separate events of different scale and the range of dips it can handle is limited by the (inherent) risk of aliasing in the tau-*p* transform.

The other two are the (multi)directional filter approach described in [8] and the Curvelet Transform approach described in [34]. Their performance has been compared in [10] and [34] and the conclusions have actually motivated the development of the Curveletiform Filter. In the CT, localization and angular resolution is limited by the order of the pyramidal decomposition while in (multi)directional filtering schemes they depend on the type and scale of the wavelet basis and the anisotropy of the filter and may vary from broad to very fine. The scheme proposed by [8] is performed by rotating the same directional filter under *adaptive control*, so that it may remain *tuned* at a given frequency or wavenumber and trained on specific traits of the data, a feat that may not always be versatile with a pyramidal decomposition. For data of moderate complexity, if wavelets with intermediate localization properties are used for multidirectional filtering, results are generally very comparable to those obtained by the CT. Nevertheless, the possibility to fine tune multidirectional filters and to choose the extent of frequency or spatial localization may be advantageous in resolving fine geometric information in very complex data. In this respect, curveletiforms offer additional efficiency because of their advantageous curvelet-like characteristics. They also offer simplicity because the problem of localization (tuning) and anisotropy is automatically addressed. For the same reason they offer superior computational efficiency because they do *not* have to be tuned under adaptive control. In consequence, their performance can match, or even improve on the performance of the multidirectional filters. In fact, a qualitative comparison of the results obtained by the CF, the CT, B-Spline wavelet filters and Gabor filters for the example of Section 3, which also appears in [8] and [34], will demonstrate that the CF, outperforms the other methods.

REFERENCES

[1] L. Jacques, L. Duval, C. Chaux, and G. Peyré, G., A panorama on multiscale geometric representations, interwining spatial, directional and frequency selectivity, Signal Processing 91 (2011) 2699-2730; doi:10.1016/j.sigpro.2011.04.025

[2] W. Freeman and F. Adelson, The design and use of steerable filters, IEEE Trans. Pattern Anal. 13 (9) (1991) 891-906.

[3] E. Simoncelli, W. Freeman, E. Adelson, and D. Heeger, D., Shiftable multiscale transforms, IEEE Trans. Inform. Theory 38 (2) (1992) 587-607.

[4] H.G. Feichtinger and T. Strohmer, Gabor Analysis and Algorithms, Birkhäuser, 1998; ISBN 0817639594

[5] H.G. Feichtinger and T. Strohmer, Advances in Gabor Analysis, Birkhäuser, 2003; ISBN 0817642390

[6] T. Lee, Image representation using 2D Gabor wavelets, IEEE Trans. Pattern Anal. 18 (10) (2008) 1-13.

[7] S.A. Little, Wavelet Analysis of Seafloor Bathymetry: An Example, in E. Foufoula-Georgiou and P. Kumar (eds.), Wavelets in Geophysics, Academic Press, San Diego, 167-182, 1994.

[8] A. Tzanis, Detection and extraction of orientation-and-scale-dependent information from two-dimensional GPR data with tuneable directional wavelet filters, Journal of Applied Geophysics 89 (2013) 48-67; doi: 10.1016/j.jappgeo.2012.11.007.

[9] C. Grigorescu, N. Petkov and M.A. Westenberg, Contour detection based on nonclassical receptive field inhibition, IEEE Trans. Image Process. 12 (7) (2003), 729-739.
[10] A. Tzanis, Signal enhancement and geometric information retrieval from 2-D GPR data with multiscale, orientation-sensitive filtering methods, First Break 32 (8) (2014) 91-98.
[11] C.K. Chui, An introduction to wavelets, Academic Press, New York, 1992.
[12] S.G. Mallat, A Wavelet Tour of Signal Processing, Academic Press, 1999.
[13] A.J. Deighan and D.R. Watts, Ground-roll suppression using the wavelet transform, Geophysics 62 (1997) 1896–1903.
[14] G.E. Leblanc, W.A. Morris and B. Robinson, Wavelet analysis approach to de-noising of magnetic data, SEG Expanded Abstract (1998) 554-557.
[15] X. Miao and S.P. Cheadle, Noise attenuation with wavelet transforms, SEG Expanded Abstract (1998) 1072-1075.
[16] M.D. Matos and P.M. Osorio, Wavelet transform filtering in the 1D and 2D for ground roll suppression, SEG Expanded Abstract (2002) 2245-2248.
[17] L., Nuzzo, and T. Quarta, Improvement in GPR coherent noise attenuation using τ - p and wavelet transforms, Geophysics 69 (2004) 789–802.
[18] Y. Jeng, C-H. Lin, Y-W. Li, C-S. Chen and H-H. Huang, Application of multiresolution analysis in removing ground-penetrating radar noise, Frontiers+Innovation – 2009 CSPG-CSEG-CWLS Convention (2009) 416-419.
[19] E. Candès, Harmonic analysis of neural networks, Appl. Comput. Harmon. Anal. 6 (1999) 197-218.
[20] E. Candès and D. Donoho, Ridgelets: A key to higher-dimensional intermittency? R. Soc. Lond. Philos. Trans. Ser. A Math. Phys. Eng. Sci. 357 (1999) 2495-2509.
[21] D. Donoho, Wedgelets: nearly minimax estimation of edges. Ann. Statistics 27 (3) (1999) 859-897.
[22] D. Donoho, and X. Huo, Beamlets and multiscale image analysis, in: T. Barth et al. (Eds.), Multiscale and Multiresolution Methods, Springer Lecture Notes in Comput. Sci. Eng., 20, (2002) 149-196.
[23] S. Mallat and G. Peyré, A review of bandlet methods for geometrical image representation, Numer. Algorithms 44 (3) (2007) 205-234.
[24] M. Do and M. Vetterli, The contourlet transform: an efficient directional multiresolution image representation IEEE Trans. Image Process. 14 (12) (2005), 2091-2106.
[25] L. Demanet and L. Ying, Wave Atoms and Sparsity of Oscillatory Patternsm Appl. Comput. Harmon. Anal. 23 (3) (2007) 368-387.
[26] Y. Lu and M. Do, Multidimensional directional filter banks and surfacelets, IEEE Trans. Image Process. 16 (4) (2007) 918-931.
[27] E. Candès and D. Donoho, Continuous curvelet transform: I. Resolution of the wavefront set, Appl. Comput. Harmon. Anal., 19 (2003), 162-197.
[28] E. Candès, and D. Donoho, Continuous curvelet transform: II. Discretization and frames, Appl. Comput. Harmon. Anal. 19 (2003), 198-222.
[29] E. Candès and L. Demanet, Curvelets and Fourier integral operators, C. R. Acad. Sci. Paris, Sér. I, 336 (5) (2003) 395–398; doi: 10.1016/S1631-073X(03)00095-5.
[30] E. Candès and D. Donoho, New tight frames of curvelets and optimal representations of objects with piecewise C^2 singularities, Comm. Pure Appl. Math. 57 (2004) 219-266.
[31] E. Candès and D. Donoho, Curvelets: new tools for limited angle tomography, Technical Report, California Institute of Technology, (2004).

[32] K. Guo and D. Labate, Optimally sparse multidimensional representation using shearlets, SIAM J. Math. Anal. 39 (2007) 298–318.
[33] J. Xu, L., Yang and D. Wu, Ripplet: a new transform for image processing, J. Vis. Commun. Image Repr. 21 (7) (2010) 627–639.
[34] A. Tzanis, The Curvelet Transform in the analysis of 2-D GPR data: Signal enhancement and extraction of orientation-and-scale-dependent information, Journal of Applied Geophysics 115 (2015) 145-170; doi: 10.1016/j.jappgeo.2015.02.015.
[35] H.F. Smith, A Hardy space for Fourier integral operators, J. Geom. Analysis 7 (1998) 629 – 653.
[36] E.J. Candès, L. Demanet, D.L. Donoho and L. Ying, Fast discrete curvelet transforms (FDCT). Multiscale Modeling and Simulation 5 (2006) 861–899.
[37] E.J. Candès, and L. Demanet, The curvelet representation of wave propagators is optimally sparse, Comm. Pure Appl. Math., 58 (11) (2005) 1472–1528.
[38] I. Daubechies, Ten lectures on Wavelets, CBMS Regional Conference Series in Applied Mathematics, SIAM, Philadelphia, PA, USA, 1992.
[39] A. Tzanis, matGPR Release 2: A freeware MATLAB® package for the analysis and interpretation of common and single offset GPR data, FastTimes 15 (1) (2010) 17 – 43.
[40] A. Roberts, Curvature attributes and their application to 3D interpreted horizons, First Break 19 (2) (2001) 85–100; doi: 10.1046/j.0263-5046.2001.00142.x.
[41] S. Chopra and J.J. Marfurt, Volumetric curvature attributes for fault/fracture characterization, First Break 25 (7) (2007) 35-46; doi: 10.3997/1365-2397.2007019.
[42] U. Theune, M.D. Sacchi and D.R. Schmitt, Least-squares local Radon Transforms for dip-dependent GPR image decomposition, Journal of Applied Geophysics, 59 (2006) 224-235; doi: 10.1016/j.jappgeo.2005.10.003.
[43] U. Theune, D. Rokosh, M.D Sacchi and D.R Schmitt, Mapping fractures with GPR: a case study from Turtle Mountain, Geophysics, 71 (5) (2006), B139-B150.
[44] S. Yang, W. Min, L. Zhao and Z. Wang, Image Noise Reduction via Geometric Multiscale Ridgelet Support Vector Transform and Dictionary Learning. IEEE Trans. Image Processing, 22 (11) (2013), 4161-4169; doi: 10.1109/TIP.2013.2271114.
[45] L. Lin, F. Liou and L. Jiao, Compressed sensing by collaborative reconstruction on overcomplete dictionary, Signal Processing, 103 (2014) 92-102; doi: 10.1016/j.sigpro.2013.11.039.